The Astrophysical Journal Letters, 994:L13 (18pp), 2025 November 20 https://doi.org/10.3847/2041-8213/ae18c2

XRISM/Resolve Reveals the Complex Iron Structure of NGC 7213: Evidence for Radial Stratification between Inner Disk and Broad-line Region

E. Kammoun[1], T. Kawamuro[2], K. Murakami[2], S. Bianchi[3], F. Nicastro[4], A. Luminari[4,5], E. Aydi[6], M. Eracleous[7], O. K. Adegoke[8], E. Bertola[9], P. G. Boorman[8], V. Braito[10,11,12], G. Bruni[5], A. Comastri[13], P. Condò[14], M. Dadina[13], T. Enoto[15], J. A. García[16,17], V. E. Gianolli[18], F. A. Harrison[8], G. Lanzuisi[13], M. Laurenti[4,14,19], A. Marinucci[20], G. Mastroserio[21], H. Matsumoto[2], G. Matt[3], G. Matzeu[22], R. Middei[4,23], E. Nardini[9], H. Noda[24], H. Odaka[2], S. Ogawa[25], F. Panessa[5], E. Piconcelli[4], C. Pinto[26], J. M. Piotrowska[8], G. Ponti[10,27,28], C. Ricci[29], R. Ricci[14,30], R. Serafinelli[4,31], F. Shi[32], D. Stern[33], A. Tanimoto[34], Y. Terashima[35], R. Tomaru[2], F. Tombesi[4,14,19], A. Tortosa[4], Y. Ueda[36], F. Ursini[3], C. Vignali[13,37], S. Yamada[38], and S. Yamada[39]

[1] Cahill Center for Astronomy & Astrophysics, California Institute of Technology, 1216 East California Boulevard, Pasadena, CA 91125, USA; ekammoun@caltech.edu
[2] Department of Earth and Space Science, Osaka University, 1-1 Machikaneyama, Toyonaka 560-0043, Osaka, Japan
[3] Dipartimento di Matematica e Fisica, Universita degli Studi Roma Tre, via della Vasca Navale 84, I-00146 Roma, Italy
[4] INAF—Osservatorio Astronomico di Roma Via Frascati, 33 I-00078 Monte Porzio Catone (RM), Italy
[5] INAF—Istituto di Astrofisica e Planetologia Spaziali, Via del Fosso del Caveliere 100, I-00133 Roma, Italy
[6] Department of Physics & Astronomy, Texas Tech University, Box 41051, Lubbock, TX 79409-1051, USA
[7] Department of Astronomy & Astrophysics and Institute for Gravitation and the Cosmos, 525 Davey Lab, 251 Pollock Road, The Pennsylvania State University, University Park, PA 16802, USA
[8] Cahill Center for Astronomy & Astrophysics, California Institute of Technology, Pasadena, 1216 East California Boulevard, CA 91125, USA
[9] INAF—Osservatorio Astrofisco di Arcetri, largo E. Fermi 5, 50127, Firenze, Italy
[10] INAF—Osservatorio Astronomico di Brera, Via Bianchi 46 I-23807 Merate (LC), Italy
[11] Department of Physics, Institute for Astrophysics and Computational Sciences, The Catholic University of America, Washington, DC 20064, USA
[12] Dipartimento di Fisica, Universitá di Trento, Via Sommarive 14, 38123 Trento, Italy
[13] INAF—Osservatorio di Astrofisica e Scienza dello Spazio (OAS) di Bologna, via P. Gobetti 93/3, I-40129 Bologna, Italy
[14] Dipartimento di Fisica, Università degli Studi di Roma "Tor Vergata," via della Ricerca Scientifica 1, I-00133 Roma, Italy
[15] Department of Physics, Kyoto University, Kitashirakawa Oiwake, Sakyo, Kyoto 606-8502, Japan
[16] X-ray Astrophysics Laboratory, NASA Goddard Space Flight Center, Greenbelt, MD 20771, USA
[17] Cahill Center for Astronomy & Astrophysics, California Institute of Technology, Pasadena, CA 91125, USA
[18] Department of Physics and Astronomy, Clemson University, Kinard Lab of Physics, Clemson, SC 29634, USA
[19] INFN—Sezione di Roma "Tor Vergata," Via della Ricerca Scientifica 1, I-00133 Roma, Italy
[20] ASI—Agenzia Spaziale Italiana, Via del Politecnico snc, 00133 Roma, Italy
[21] Scuola Universitaria Superiore IUSS Pavia, Palazzo del Broletto, piazza della Vittoria 15, I-27100 Pavia, Italy
[22] European Space Agency (ESA), European Space Astronomy Centre (ESAC), 28691 Villanueva de la Cañada, Madrid, Spain
[23] Space Science Data Center, Agenzia Spaziale Italiana, Via del Politecnico snc, 00133 Roma, Italy
[24] Astronomical Institute, Tohoku University, Miyagi 980-8578, Japan
[25] Institute of Space and Astronautical Science (ISAS), Japan Aerospace Exploration Agency (JAXA), Kanagawa 252-5210, Japan
[26] INAF/IASF Palermo, via Ugo La Malfa 153, I-90146 Palermo, Italy
[27] Max-Planck-Institut für extraterrestrische Physik, Gießenbachstraße 1, 85748, Garching, Germany
[28] Como Lake Center for Astrophysics (CLAP), DiSAT, Università degli Studi dell'Insubria, via Valleggio 11, 22100 Como, Italy
[29] Department of Astronomy, University of Geneva, ch. d'Ecogia 16, 1290, Versoix, Switzerland
[30] INAF-Istituto di Radioastronomia, Via Gobetti 101, I-40129 Bologna, Italy
[31] Instituto de Estudios Astrofísicos, Facultad de Ingeniería y Ciencias, Universidad Diego Portales, Avenida Ejército Libertador 441, Santiago, Chile
[32] Shanghai Astronomical Observatory, Chinese Academy of Science, No.80 Nandan Road, Shanghai, People's Republic of China
[33] Jet Propulsion Laboratory, California Institute of Technology, Pasadena, CA 91109, USA
[34] Graduate School of Science and Engineering, Kagoshima University, Kagoshima, 890-8580, Japan
[35] Department of Physics, Ehime University, Ehime 790-8577, Japan
[36] Department of Astronomy, Kyoto University, Kyoto 606-8502, Japan
[37] Dipartimento di Fisica e Astronomia "Augusto Righi," Università degli Studi di Bologna, via P. Gobetti 93/2, 40129 Bologna, Italy
[38] Frontier Research Institute for Interdisciplinary Sciences, Tohoku University, Sendai 980-8578, Japan
[39] Department of Physics, Rikkyo University, 3-34-1 Nishi Ikebukuro, Toshima-ku, Tokyo 171-8501, Japan

Received 2025 October 2; revised 2025 October 27; accepted 2025 October 27; published 2025 November 13

Abstract

We present the first high-resolution X-ray spectrum of NGC 7213 obtained with XRISM/Resolve, supported by simultaneous XMM-Newton, NuSTAR, and SOAR optical data. The XRISM spectrum resolves the neutral Fe Kα into two components: a narrow core (FWHM $= 650^{+240}_{-220}$ km s^{-1}), consistent with emission at the dust sublimation radius, and a broader asymmetric line, best described by disklike emission from $\sim 100\,R_{\rm g}$. This disk component mirrors the profile of the double-peaked Hα line observed in the optical. In addition, we detect broadened Fe XXV and Fe XXVI emission lines, whose inferred locations bridge the gap between the inner disk and the optical broad-line region. The weak narrow Fe Kα equivalent width (EW $= 32 \pm 6$ eV) and the absence of a Compton hump imply a low-covering-fraction, Compton-thin torus. Together, these results reveal a radially stratified structure in

NGC 7213, spanning nearly 4 orders of magnitude in radius, and place the source in an intermediate-accretion state ($\lambda_{\rm Edd} = 0.1\%–1\%$), where the inner disk and broad-line region remain, while the torus shows signs of dissipation.

Unified Astronomy Thesaurus concepts: Active galactic nuclei (16); Low-luminosity active galactic nuclei (2033); X-ray active galactic nuclei (2035); Black holes (162)

1. Introduction

One of the main observational signatures of active galactic nuclei (AGNs) is the broadening of atomic emission lines by the high-velocity motion of gas near the central supermassive black hole (SMBH). Over decades, extensive efforts have been dedicated to characterizing the broad-line region (BLR) emission lines, kinematics, and ionization structure, informing the interplay between the SMBH and its surrounding gas. BLR observations can also constrain the mechanism for transporting gas inward through accretion disks or outward through winds (J. H. Krolik 2001). The source of the broad emission lines has been associated in a variety of works with the surface of the accretion disk or a wind arising at the surface of the outer accretion disk (e.g., S. Collin-Souffrin 1987; S. Collin-Souffrin et al. 1988; R. T. Emmering et al. 1992; N. Murray & J. Chiang 1997; A. Baskin & A. Laor 2018; M.-H. Naddaf et al. 2021, and references therein). A characteristic length scale for the BLR is commonly estimated by measuring the delay between the variations of brightness of the accretion disk continuum and the corresponding variations of the broad emission lines (known as reverberation mapping; R. D. Blandford & C. F. McKee 1982). Directly imaging such regions has been challenging because of their small angular size ($\lesssim$0.1 mas). It is only very recently that the BLR could be spatially resolved in a handful of bright nearby AGNs, thanks to the development of a new generation of optical/near-infrared (O/NIR) interferometers (GRAVITY Collaboration et al. 2024). However, despite the wealth of knowledge gained from UV/O/NIR observations, a comprehensive understanding of the BLR's complex dynamics and ionization processes remains elusive.

Studying the BLR has predominantly been conducted using UV/O spectroscopy. In X-rays, the Fe Kα line could be spectroscopically resolved in a limited number of bright AGNs using the Chandra High-Energy Transmission Grating (HETG). Chandra/HETG observations suggest that there is no universal location of the Fe Kα line-emitting region relative to the optical BLR. In general, a given source may have contributions to the Fe Kα line originating at parsec-scale distances from the SMBH, down to distances a factor of $\sim$2 closer to the SMBH than the BLR Hβ (T. Yaqoob et al. 2001; X. W. Shu et al. 2010). Only in a few cases has it been possible to show that the Fe Kα line width measured by Chandra/HETG is produced in the optical BLR (S. Bianchi et al. 2008; X. W. Shu et al. 2010; J. M. Miller et al. 2018). Recent studies have shown that, for local AGNs, the Fe Kα emitting region size is smaller than the dust sublimation radius in the majority of the sources (e.g., P. Gandhi et al. 2015; C. Andonie et al. 2022). The Resolve X-ray spectrometer on board the X-ray Imaging and Spectroscopy Mission (XRISM; M. Tashiro et al. 2024) is providing an unprecedented look at the BLR in X-rays (e.g., Xrism Collaboration et al. 2024; D. Bogensberger et al. 2025; J. M. Miller et al. 2025).

Over the last three decades, an increasing number of AGNs have been found to exhibit long-lived broad ($\sim$10,000 km s^{-1}) double-peaked Balmer emission lines (e.g., M. Eracleous & J. P. Halpern 1994, 2003; I. V. Strateva et al. 2003; T. Storchi-Bergmann et al. 2017; C. Ward et al. 2025). These lines are commonly modeled as emission from a relativistic Keplerian disklike structure, where Doppler boosting results in asymmetry between the red and blue peaks (see, e.g., K. Chen & J. P. Halpern 1989; K. Chen et al. 1989; T. Storchi-Bergmann et al. 1993; M. Eracleous & J. P. Halpern 1994, 2003; I. V. Strateva et al. 2003; S. Bianchi et al. 2019, 2022; C. Ward et al. 2024, 2025). M. Eracleous & J. P. Halpern (1994) estimated that double-peaked emitters make up $\sim$15% of radio-loud AGNs at $z < 0.4$. I. V. Strateva et al. (2003) estimated that double-peaked emitters make up $\sim$4% of the Sloan Digital Sky Survey (mostly radio-quiet) quasar population at $z < 0.4$, while C. Ward et al. (2025) estimated that double-peaked emitters make up $\sim$21% of all X-ray-selected low-redshift AGNs at $z < 0.3$ in the Berkeley Automated Supernova Search sample. Some of these sources show substantial changes in the relative flux of the blue and red peaks over timescales of months to years, which is well modeled by the rotation of spiral arms or hot spots in the disk (e.g., S. Gezari et al. 2007; K. T. Lewis et al. 2010; C. Ward et al. 2024). If these double-peaked features originate from the accretion disk, we should expect to see analogous Fe lines in the X-ray spectra of these sources.

1.1. NGC 7213

Located at a distance of 22.8 Mpc, the nearly face-on spiral galaxy NGC 7213 harbors an intermediate-/low-luminosity AGN powered by a BH with a mass of $8^{+16}_{-6} \times 10^7\,M_\odot$ (derived using velocity dispersion; A. Schnorr-Müller et al. 2014), accreting at $\sim$0.05%–1% of its Eddington limit. NGC 7213 has been proposed as a high-mass analog of hard-state X-ray binaries (XRBs; D. Emmanoulopoulos et al. 2012), showing a "harder when brighter" behavior. The source lies between the radio-loud and radio-quiet regimes, showing no extended radio emission. M. E. Bell et al. (2011) showed that the X-ray and radio light curves of the source are correlated, with the radio variability lagging behind the X-rays by 24 days (48 days) at 8.4 GHz (4.8 GHz). The available data suggest that the source could either be analogous to radio-loud AGNs, where the jet is powered by an advection-dominated accretion flow, or it is similar to a hard-state XRB with a truncated accretion disk.

S. Bianchi et al. (2008) described the Chandra/HETG spectrum with a power law ($\Gamma = 1.69 \pm 0.01$) and three emission lines. The strongest of these lines is consistent with a neutral Fe Kα at $6.397^{+0.006}_{-0.011}$ keV with an FWHM of FWHM $= 2400^{+1100}_{-600}$ km s^{-1} ($\sigma = 22^{+10}_{-6}$ eV) and an equivalent width (EW) of EW $= 120^{+40}_{-30}$ eV. The broadening of this line is consistent with the value measured for the broad Hα emission line of 2640^{+110}_{-90} km s^{-1}. In addition, two ionized Fe lines consistent with the He-like Fe XXV and H-like Fe XXVI are hinted at in the Chandra/HETG spectrum. S. Bianchi et al. (2008) reported a tentative blueshift of the Fe XXV and

Fe XXVI lines by around 1000 km s^{-1}, which they interpret as a possible indication of starburst winds. F. Shi et al. (2022) attributed this tentative blueshift to hot winds from the accretion flow (see also F. Shi et al. 2024).

XMM-Newton and Suzaku observations of the source confirmed the Chandra/HETG results, albeit at lower resolution (A. P. Lobban et al. 2010). The broadening and the EW of the low-ionization Fe K line both suggest that this line originates from Compton-thin gas at a distance consistent with the BLR, although with large uncertainties. Interestingly, the NuSTAR observation of NGC 7213 showed that its hard-X-ray spectrum can be described by a power law with a high-energy cutoff, showing no signature of a Compton hump (F. Ursini et al. 2015). This further supports the conclusion that the low-ionization Fe K line is produced by Compton-thin material with an equivalent hydrogen column density $N_{\rm H} = 5.0^{+2.0}_{-1.6} \times 10^{23}$ cm^{-2}.

The optical spectrum of NGC 7213 revealed the presence of a double-peaked broad (DPB) Hα emission line in addition to the regular symmetric BLR-like line (A. Schnorr-Müller et al. 2014; J. S. Schimoia et al. 2017). J. S. Schimoia et al. (2017) studied the variability of the Hα complex and showed that both parts of the line profile are variable. The authors estimated the evolution timescale of the symmetric part to be of ∼7–21 days and that of the DPB part to be of the order of a few months. This suggests that the symmetric part evolves on a light-travel timescale (consistent with the distance between the BLR and the central engine), while the DPB part is more dominated by slower dynamical timescales. They modeled the DPB part assuming that it originates from a region of a Keplerian and relativistic accretion disk. Their model resulted in an DPB emitting region between ∼300 $R_{\rm g}$ and 3000 $R_{\rm g}$, where $R_{\rm g} = GM_{\rm BH}/c^2$ is the gravitational radius, with an inclination of 47° ± 2°. Within the context of their model, the disk harbors a spiral arm with varying contrast relative to the underlying disk, which processes cause the variability in the DPB part of the profile.

In this Letter, we present the first high-spectral-resolution observation of NGC 7213 with XRISM. Simultaneous observations with XMM-Newton, NuSTAR, and other ground-based facilities have been performed to support the XRISM observation. In this first Letter, we focus on the Fe line region (∼6–7 keV range), employing mainly phenomenological models. Follow-up papers will discuss in greater detail the broadband aspect of these spectra as well as test a variety of physically motivated models.

In Section 2, we present the details of the observation and the data reduction procedures. The results of the spectral analysis are described in Section 3. We discuss our findings and their implications in Section 4. We present our conclusions in Section 5.

2. Observations and Data Reduction

2.1. XRISM Observation

XRISM observed NGC 7213 on 2024 November 4–7 for a total of 118.5 ks (ObsID 201115010; PIs: E. Kammoun and T. Kawamuro). XRISM is a JAXA/NASA collaborative mission, with ESA participation, consisting of two instruments: a high-resolution spectrometer (Resolve; Y. Ishisaki et al. 2025) and a soft-X-ray imaging spectrometer (Xtend; H. Noda et al. 2025). The Resolve and Xtend instruments were operated in "PX_NORMAL" mode and "1/8 window" mode, respectively. In this work, we focus only on the Resolve data. We defer the full analysis of the Xtend data to a subsequent paper.

We reprocessed the Resolve data using the XAPIPELINE command and the latest calibration files (CALDB 11, released on 2025 March 11). We produced the Level 2 cleaned files following the XRISM data reduction "ABC Guide,"[40] v1.0. We applied the recommended screening for the pulse rise time, event type, and status. In addition, we excluded the events from pixel number 27, as recommended to avoid calibration uncertainties. We also applied a filter of the geomagnetic cutoff rigidity (COR), which is roughly inversely proportional to the particle background in low Earth orbits. We tested different COR thresholds and we confirmed that the results did not significantly change, as discussed in Appendix A. We used a threshold of COR > 6, which reduced the net exposure time to 90.3 ks. Our choice can be considered as a reasonable compromise between the exposure time and signal-to-noise ratio (S/N). We selected only the high-resolution events (Hp), which accounted for 95.2% of all the events during this observation.

We used the XSELECT task to extract spectra and light curves. Then we used the RSLMKRMF command to generate the extra-large type of response file for Resolve. Next, we created a standard exposure map for both instruments using the XAEXPMAP command. We finally created the ancillary response file (ARF) using the XAARFGEN command. This command runs a ray-tracing simulation, to calculate the reflection and transmission of photons from the assumed X-ray source and to count the photons detected in the selected pixels. We set the number of photons in the simulations NUMPHOTON = 600,000 and limited the ARF to the 2–10 keV range. Given the brightness of the source and the low non-X-ray background (NXB) of Resolve, we can safely neglect the NXB during the spectral fits. As a check, we verified that no signatures of the known NXB lines appeared in the spectrum of the source.

2.2. XMM-Newton Observations

Two XMM-Newton Director's Discretionary Time (DDT) observations of NGC 7213 took place on 2024 November 5 and on 2024 November 6 (ObsIDs 0953012201 and 0953012301, respectively; PI: E. Kammoun), for total exposure times of 47.4 and 56.4 ks, respectively. We refer to these observations as XMM-Newton ObsA and ObsB, respectively, hereafter. A problem in the communication with the ground station occurred during the first observation, which resulted in a shorter exposure. The observations were operated in the Large Window/Thin Filter mode for EPIC-pn (L. Strüder et al. 2001) and in Small Window/Thin Filter mode for the two EPIC-MOS (M. J. L. Turner et al. 2001) instruments. In this work, we focus on the EPIC-pn data only.[41] We use the XMM-Newton Science Analysis System (SAS V22.1.0) to reduce and analyze the data of these observations. Source spectra and light curves were extracted from an annular region with an inner radius of 10″ and an outer radius of 35″ centered

---

[40] https://heasarc.gsfc.nasa.gov/docs/xrism/analysis/abc_guide/xrism_abc.html

[41] The EPIC-MOS and EPIC-pn spectra are consistent. For the purposes of this work, including the EPIC-MOS spectra does not affect any of the conclusions.

on the source, to reduce pileup. The corresponding background spectra were extracted from an off-source circular region located on the same CCD chip, with a radius of 75″. We filtered out periods with strong background flares. This resulted in net exposures of 9.9 ks and 29.6 ks, respectively. Response matrices were produced using FTOOLSRMFGEN and ARFGEN. The XMM-Newton light curves do not show any significant variability.

2.3. NuSTAR Observation

A NuSTAR DDT observation of NGC 7213 took place on 2024 November 5 (ObsID 91001636002; PI: E. Kammoun) for a total exposure of 52 ks. The data were reduced using the standard pipeline in the NuSTAR Data Analysis Software (NUSTARDAS V2.1.4), using CALDB 20241104. We cleaned the unfiltered event files with the standard depth correction. We reprocessed the data using the SAAMODE = OPTIMIZED, SAACALC=3, and TENTACLE = YES criteria for a more conservative treatment of the high background levels near the South Atlantic Anomaly. We used the OPTIMAL-RADIUS tool in NUSTAR-GEN-UTILS (B. Grefenstette et al. 2025) to estimate the optimal source region to maximize the S/N above 10 keV. Thus, we extracted the source and background light curves and spectra from circular regions of radii 51″ and 90″, respectively, for the two focal plane modules (FPMA and FPMB), using the HEASOFT task NUPRODUCTS. In the following, we analyze the spectra from FPMA and FPMB jointly, without combining them. All X-ray spectra in this work were binned using the ftool FTGROUPPHA with optimal binning (J. S. Kaastra & J. A. M. Bleeker 2016).

2.4. Southern Astrophysical Research Telescope Observation

On 2024 November 2, we obtained medium-resolution optical spectroscopy for NGC 7213 using the Goodman spectrograph (J. C. Clemens et al. 2004) on the 4.1 m Southern Astrophysical Research (SOAR) telescope located on Cerro Pachón, Chile. We used a setup with a 2100 l mm^{-1} grating and a 0″.95 slit, yielding a resolution $R \approx 5000$ in a region centered on Hα and Hβ that is 570 Å wide. The spectra were reduced and optimally extracted using the APALL package in IRAF (D. Tody 1986). In this work, we focus on the Hα region. The results from the Hβ are broadly consistent with the findings of the Hα, but they require a more careful treatment of the Fe II pseudo-continuum emission, which is beyond the scope of this work. In the rest of the Letter, we adopt the redshift of the source to be $z = 0.005839$, as reported for 21 cm estimates by the NASA/IPAC extragalactic database.

3. Analysis and Results

In this section, we present the results obtained by modeling the spectra from the different instruments. The X-ray spectral analysis is performed using XSPECV12.15.0D (K. A. Arnaud 1996). We adopt the Cash statistic (C-stat; W. Cash 1979). All uncertainties are reported at the 90% confidence level, unless specified otherwise.

3.1. X-Ray Continuum Fitting

To model the continuum spectrum of the source, we fit the data in the 2–10 keV range for XRISM/Resolve, in the 0.5–10 keV range for XMM-Newton/EPIC-pn, and in the 3–60 keV range for NuSTAR/FPMA and FPMB. For all instruments, we ignored the 6–8 keV energy range, to avoid the complexity introduced by the presence of the Fe emission lines. This exclusion is not expected to affect the continuum fit. We adopt a model that consists of an absorbed power law with a high-energy cutoff. The spectra and the best-fit model are presented in the top panel of Figure 1. The column density of the interstellar absorber is fixed to the Galactic value of $N_{\mathrm{H}} = 1.08 \times 10^{20}\ \mathrm{cm}^{-2}$ (HI4PI Collaboration et al. 2016). We tied all the parameters among the five spectra, including a cross-calibration normalization constant. We fixed this constant to the one for XRISM/Resolve and let it vary for all the other spectra. The spectra are well fitted with this model, with

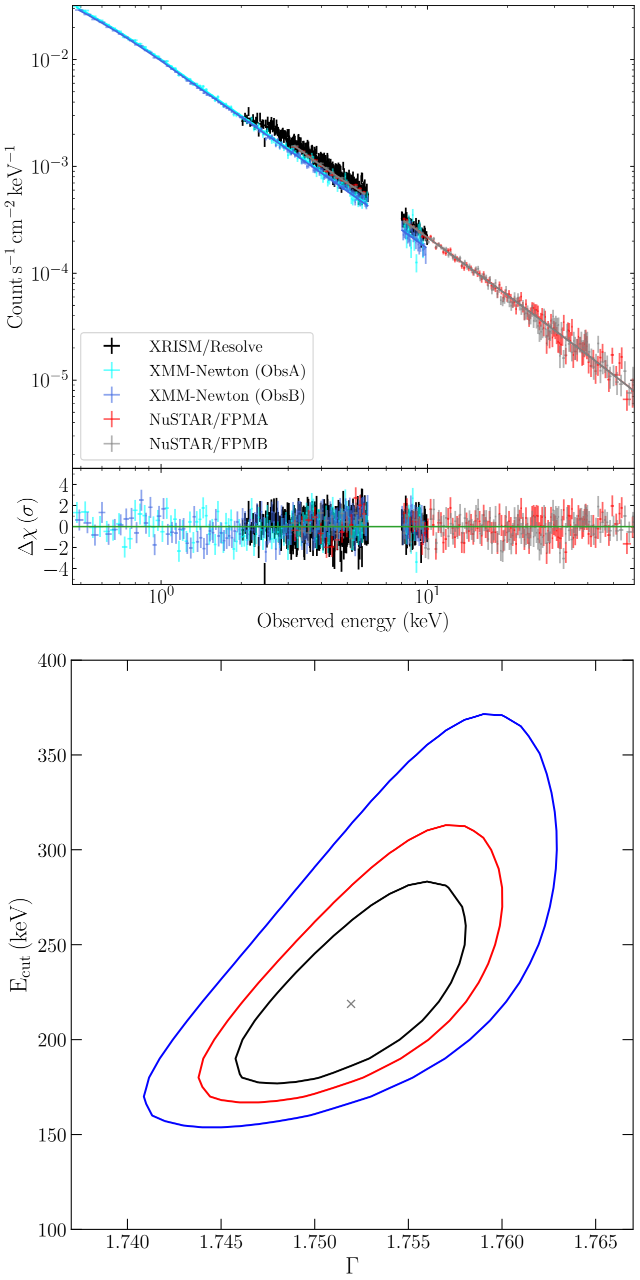

Figure 1. Top: XRISM/Resolve (black), XMM-Newton/EPIC-pn, and NuSTAR spectra modeled with an absorbed power law with a high-energy cutoff. We also show the corresponding residuals. Bottom: the high-energy cutoff versus photon index confidence regions at the 68%, 95%, and 99% levels (black, red, and blue, respectively).

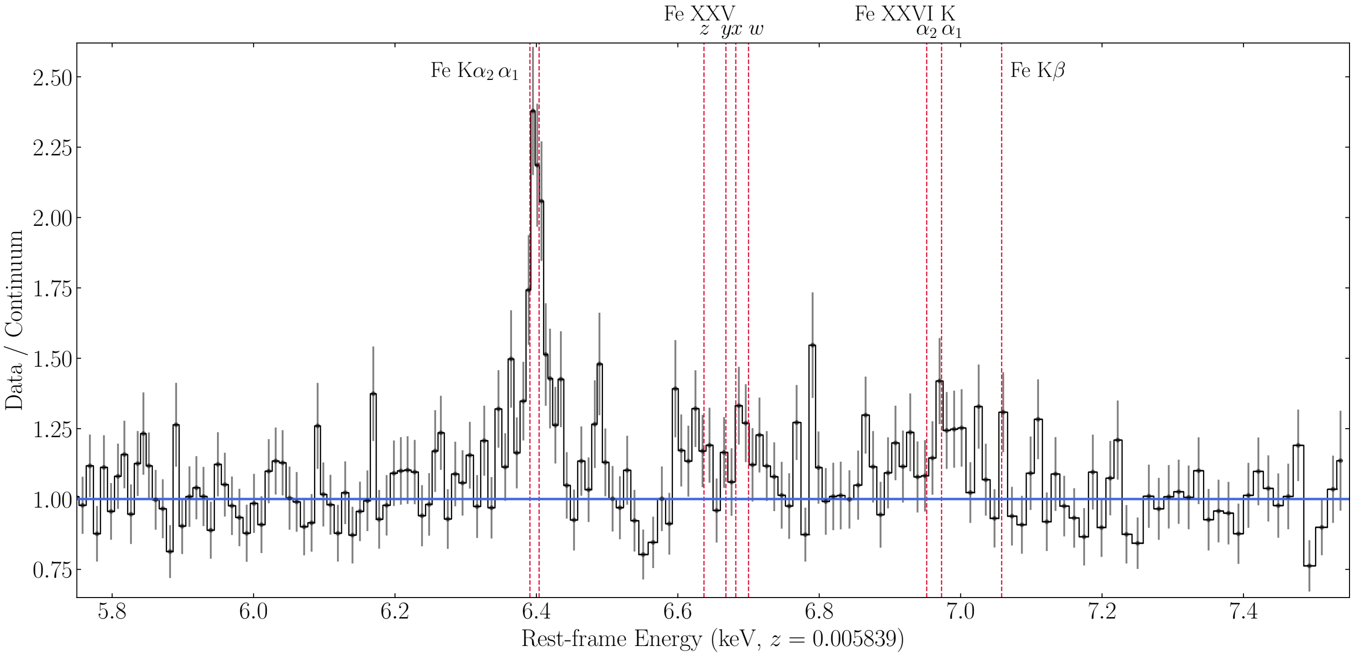

Figure 2. Data-to-continuum ratio of the XRISM/Resolve spectrum in the Fe line region in the observed frame. The red dashed lines show the expected energies for the low-ionization Fe K$\alpha_{1,2}$ and Kβ lines and the high-ionization Fe XXV (w, x, y, z) and Fe XXVI K$\alpha_{1,2}$ lines.

a C − stat/dof = 2410/2341. We obtained a best-fit photon index $\Gamma = 1.752 \pm 0.006$, a high-energy cutoff $E_{\rm cut} = 220^{+60}_{-40}$ keV, and a 2–10 keV flux $F_{2\text{–}10\,\rm keV} = 4.74 \pm 0.05 \times 10^{-11}$ erg s^{-1} cm^{-2}. The bottom panel of Figure 1 shows the $E_{\rm cut}$ versus Γ confidence contours. We obtained cross-normalization constants of 1.04 ± 0.01 for NuSTAR FPMA/FPMB and 0.81 ± 0.01 and 0.78 ± 0.01 for XMM-Newton[42] ObsA and ObsB, respectively. Assuming a luminosity distance of 22.8 Mpc, the intrinsic 2–10 keV luminosity of the source is $(2.95 \pm 0.03) \times 10^{42}$ erg s^{-1}. Thus, for a bolometric correction $\kappa_{\rm X} = L_{\rm bol}/L_{2-10} = 10$ obtained from the relation provided by F. Duras et al. (2020) and I. E. López et al. (2024), we find an Eddington ratio $\lambda_{\rm Edd} = L_{\rm bol}/L_{\rm Edd} = 0.001$–$0.01$, given the uncertainty on the BH mass in this source. During these observations, the source is caught in its brightest state since the 1980s (Z. Yan & F.-G. Xie 2018), being ~two times brighter than the Chandra/HETG observation. The harder photon index than previously reported is consistent with the "harder when brighter" behavior in this source (D. Emmanoulopoulos et al. 2012).

3.2. The Fe Line Region

In this section, we focus on the fit to the region of the Fe emission lines. We model the XRISM/Resolve spectra only, in the 5.7–7.5 keV range in the observed frame. We assume the continuum follows the best-fit model derived in the previous section. We fix the photon index and the high-energy cutoff to their best-fit values, and we leave the normalization of the power law free to vary. In Figure 2, we show the ratio of the XRISM/Resolve data to the continuum. This figure clearly shows an excess in emission centered around the expected energies for the neutral Fe K$\alpha_{1,2}$ doublets and a hint of excess at the expected energy for the Fe Kβ line. We also see an excess in emission at the expected energies for Fe XXV and Fe XXVI. The neutral Fe Kα line shows a clear narrow core with a broader asymmetric base. The Fe XXV and Fe XXVI lines appear at a lower intensity with an apparent broadening. We note that we examined the data for intra-observation variability. However, no strong variability could be confirmed. We found only a $\sim 2\sigma$ hint of variability in the intensity of the neutral Fe Kα emission line. Thus, we analyze the time-integrated spectrum in the rest of the Letter.

First, we modeled the Fe K$\alpha_{1,2}$ by adding the ZFEKLOR model in XSPEC, which consists of seven Lorentzian approximations to the line profile of Fe K fluorescence from neutral material (G. Hölzer et al. 1997), at the rest frame of the source. In addition, we added a Gaussian line at the rest-frame energy of the neutral Fe Kβ (7.06 keV) for completeness, leaving the normalizations of both lines free to vary. We also smoothed the lines with a Gaussian profile, using the GSMOOTH model in XSPEC. This improved the fit by $\Delta C = -188$ for two additional free parameters, resulting in an FWHM of the Fe K line of 1300 km s^{-1} ($\sigma = 11$ eV). However, additional residuals were still present blueward and redward of the Fe K line, implying the presence of a second broader line. Thus, we added an additional broadened GSMOOTH × ZFEKLOR line, which improved the fit by $\Delta C = -14$ for two additional free parameters. We obtained an FWHM of 4500^{+5500}_{-2200} km s^{-1} ($\sigma = 41$ eV) and a line intensity of $(1.5 \pm 0.6) \times 10^{-5}$ photon s^{-1} cm^{-2}. This reduced the FWHM of the narrow line to 650 km s^{-1}. We then added a series of four Gaussian (ZVGAUSSIAN) emission lines, assuming the rest-frame energies of the Fe XXV as resonant (w, at $E_{\rm rest} = 6.700$ keV), intercombination (x, at $E_{\rm rest} = 6.682$ keV; and y, at $E_{\rm rest} = 6.668$ keV), and forbidden (z, at $E_{\rm rest} = 6.637$ keV). We assumed the same broadening for all these lines. The intensities of the intercombination lines were low and unconstrained, so we fixed them to zero. The addition of the Fe XXV lines improved the fit by $\Delta C = -25$ for three

---

[42] A cross-calibration difference of ~18%–20% is already expected between XMM-Newton and NuSTAR, as detailed in the XMM-Newton release note XMM-CCF-REL-388: https://xmmweb.esac.esa.int/docs/documents/CAL-SRN-0388-1-4.pdf.

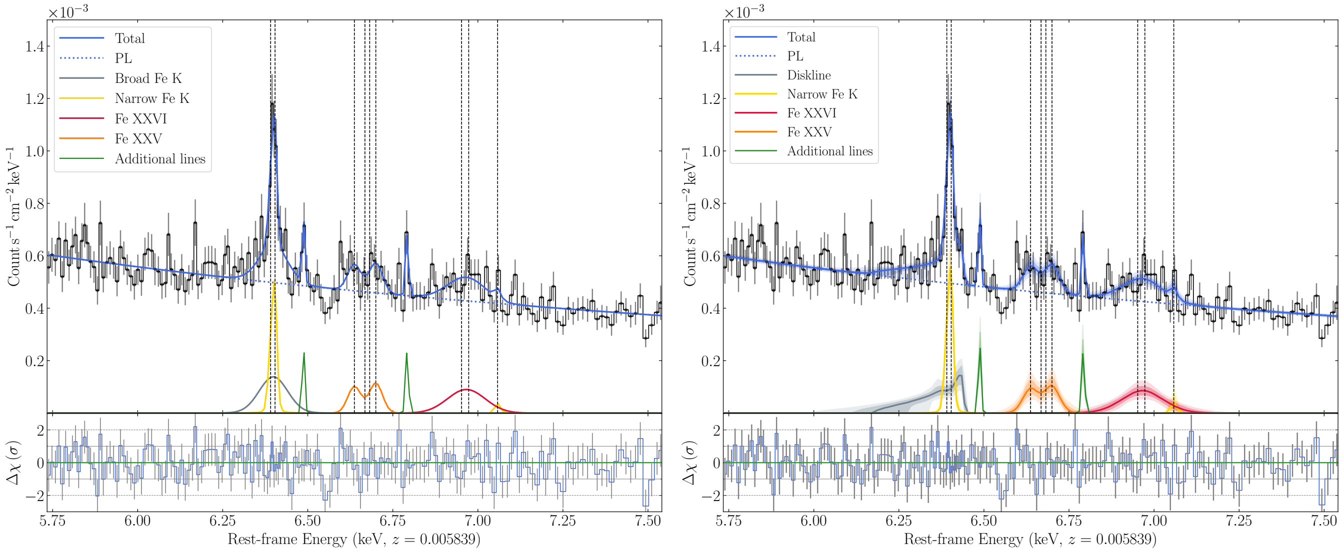

Figure 3. Modeling the XRISM/Resolve spectrum (focusing on the Fe region). In addition to the continuum (blue dotted line), we also show the narrow and broad Fe Kα lines (yellow and gray, respectively), the Fe XXV emission lines (orange), the Fe XXVI lines (red), and two Gaussian emission lines added at 6.45 and 6.75 keV (green). The left panel shows the best fit assuming that the broad Fe Kα is described with a ZFEKLOR model smoothed with a Gaussian profile. The right panel shows the best fit assuming that the broad Fe Kα is described with a DISKLINE model. The results in the right panel are based on MCMC analysis. The solid lines and the shaded region correspond to the median profile and the 68% and 95% credibility envelopes of each spectral component, respectively.

additional free parameters (the intensities of the w and z lines and the common FWHM). We obtained an FWHM of the Fe XXV lines of 2030 km s^{-1}. Then, we added two Gaussian lines (ZVGAUSSIAN) at the rest-frame energies of the Fe XXVI Kα_1 and Kα_2 lines (6.973 keV and 6.952 keV, respectively), assuming an intensity ratio of 2:1. We also assumed a common broadening for the two lines that is independent of that of the Fe XXV lines. The addition of these two lines improved the fit by $\Delta C = -21$ for two more free parameters. We note that allowing the energies of all these lines to shift did not result in any significant improvement. All the lines are consistent with the rest frame of the source. Finally, we considered adding two Gaussian lines to account for the narrow excess seen at ∼6.45 and ∼6.75 keV. We assumed that both lines are unresolved. The addition of these two lines improved the fit by $\Delta C = -15$ and -14, respectively, for one additional free parameter each. The observed energies of these two lines are 6.449 keV and 6.753 keV, corresponding to rest-frame energies of 6.489 keV and 6.794 keV, respectively, assuming that the lines are emitted by NGC 7213. The possible origin of these lines is discussed in Section 4.4. In the following, we fix the lines at their best-fit energies, leaving only their corresponding normalizations free. After including all these spectral components, the best-fit statistics obtained are $C/\mathrm{dof} = 517/516$. The best-fit model is shown in the left panel of Figure 3. The model in XSPEC can be expressed as follows:

$$\begin{aligned}\mathrm{MODEL} = {} & \mathrm{ZPOWERLAW} \\ & + \mathrm{GSMOOTH} \times (\mathrm{ZFEKLOR}_{\mathrm{FeK}\alpha} + \mathrm{ZGAUSS}_{\mathrm{FeK}\beta})_n \\ & + \mathrm{GSMOOTH} \times \mathrm{ZFEKLOR}_{\mathrm{FeK}\alpha,\mathrm{b}} \\ & + 2 \times \mathrm{ZGAUSS}_{\mathrm{Fe\,XXV}} + 2 \times \mathrm{ZGAUSS}_{\mathrm{Fe\,XXVI}} \\ & + \mathrm{GAUSS}_{6.45\,\mathrm{keV}} + \mathrm{GAUSS}_{6.75\,\mathrm{keV}}.\end{aligned} \tag{1}$$

The "n" and "b" subscripts indicate the narrow and the broad low-ionization Fe Kα lines.

A Gaussian line profile cannot fully account for the apparent asymmetry in the broad Fe Kα line. To account for this, we replaced (GSMOOTH × ZFEKLOR$_{\mathrm{FeK}\alpha,\,\mathrm{b}}$) in Equation (1) with a DISKLINE model, which considers line emission from a relativistic accretion disk (A. C. Fabian et al. 1989). The model in XSPEC can be expressed as follows:

$$\begin{aligned}\mathrm{MODEL} = {} & \mathrm{ZPOWERLAW} \\ & + \mathrm{GSMOOTH} \times (\mathrm{ZFEKLOR}_{\mathrm{FeK}\alpha} + \mathrm{ZGAUSS}_{\mathrm{FeK}\beta})_n \\ & + \mathrm{DISKLINE} \\ & + 2 \times \mathrm{ZGAUSS}_{\mathrm{Fe\,XXV}} + 2 \times \mathrm{ZGAUSS}_{\mathrm{Fe\,XXVI}} \\ & + \mathrm{GAUSS}_{6.45\,\mathrm{keV}} + \mathrm{GAUSS}_{6.75\,\mathrm{keV}}.\end{aligned} \tag{2}$$

In addition to the line energy, which we fixed at 6.4 keV in the rest frame of the source, the model's parameters are the inner edge of the disk (R_{in}), the outer edge of the disk (R_{out}), the disk radial emissivity index[43] (q), and the inclination (i). The emissivity index could not be constrained when we let it vary ($q > 0.1$). This limit is consistent with the "standard" emissivity index of 3, expected in the disk at large radii. Indeed, for an optically thick and geometrically thin α-disk, the thermal energy dissipation per unit surface area is proportional to r^{-3}. Also, for a compact central X-ray corona, the irradiation at distant parts of the accretion disk should follow r^{-3} (see, e.g., C. S. Reynolds & M. C. Begelman 1997). Thus, we fitted the XRISM/Resolve spectrum by fixing q at 3. We also fixed the outer radius at $R_{\mathrm{out}} = 5000\,R_{\mathrm{g}}$ because the fit was not sensitive to the value of R_{out}. This fit resulted in $C/\mathrm{dof} = 510/515$, an improvement by $\Delta C = -7$ for one more free parameter compared to a Gaussian (an overall improvement of $\Delta C = -21$ with respect to the fit with no broad line). To test the goodness of the fit, we use the analytic prescription provided by J. S. Kaastra (2017) to estimate the expected

---

[43] DISKLINE assumes that the emissivity of the disk follows a power-law profile $\epsilon(r) \propto r^{\mathtt{Betor10}}$, where `Betor10` $= -q$.

C-stat and its variance based on the observed spectrum. We find an expected C-stat of 533 ± 33. Thus, our best-fit C-stat is consistent with the expected value within less than 1σ. To sample the posterior distribution of the XRISM/Resolve spectral model, we employed XSPEC's implementation of the Goodman–Weare affine-invariant ensemble sampler, using 64 walkers and 4×10^6 accepted steps per walker. The first 10^6 steps were discarded as burn-in. The convergence tests and uncertainty estimates are detailed in Appendix B.

In addition, we ran a set of simulations, detailed in Appendix C, to assess the significance of the emission lines with relatively low ΔC used in our model. While the significance of a broad base of the low-ionization Fe Kα line is strong, we tested the significance of an asymmetric DISKLINE with respect to a symmetric Gaussian-broadened line. We found that given the quality of our data, the DISKLINE is preferred with 99.1% confidence (2.6σ). As for the lines at 6.45 and 6.75 keV, we find that they are both significant with 99.9% confidence ($\sim 3.3\sigma$).

Our results demonstrate for the first time in NGC 7213 that the Fe Kα is consistent with being composed of two lines: a narrow core with FWHM = 650^{+240}_{-220} km s^{-1} and a broader line that is consistent with a disklike emission originating at a distance of $\sim 100\,R_g$ (~ 0.03–3×10^{-3} pc, given the uncertainty of the BH mass). Our best-fit model results in a low inclination of 11° that is consistent with the unobscured properties and the optical classification of this source. In addition, the high resolution of the XRISM/Resolve spectrum allowed us to resolve the forbidden and the resonant lines of Fe XXV, which are broadened with FWHM = 2350^{+1600}_{-900} km s^{-1}. In addition, we found an even broader Fe XXVIK$\alpha_{1,2}$ doublet with FWHM = 6100^{+2500}_{-2300} km s^{-1}. The best-fit parameters obtained using this model are listed in Table 1.

Table 1
Best-fit Parameters Obtained by Fitting the XRISM/Resolve Spectrum

Spectral component	Parameter		ΔC
Narrow Fe Kα	FWHM	650^{+240}_{-220}	−188
	Norm$_{\rm Fe\ K\alpha}$	$14.3^{+2.4}_{-2.8}$	
	Norm$_{\rm Fe\ K\beta}$	<1.6	
	EW	32 ± 6	
DISKLINE	i [deg]	$11.3^{+2.2}_{-0.9}$	−21
	$\log(R_{\rm in}/R_g)$	$2.0^{+0.5}_{-0.4}$	
	Norm	16^{+6}_{-7}	
	EW	26 ± 18	
Fe XXV	FWHM	2350^{+1600}_{-900}	−25
	Norm$_{\rm f}$	5.4 ± 2.6	
	Norm$_{\rm r}$	5.9 ± 2.4	
	EW$_{\rm f}$	10 ± 5	
	EW$_{\rm r}$	11 ± 5	
Fe XXVI	FWHM	6100^{+2500}_{-2300}	−21
	Norm$_{\rm K\alpha1}$	8.9 ± 3.1	
	EW$_{\rm K\alpha1}$	20 ± 6	
Gaussian lines	Norm$_{E\,=\,6.45\ \rm keV}$	2.5 ± 0.9	−15
	Norm$_{E\,=\,6.75\ \rm keV}$	2.2 ± 0.9	−14

Note. The last column shows the improvement in C-stat obtained by introducing each of the lines. FWHMs are in units of kilometers per second. Normalizations are in units of 10^{-6} photon s^{-1} cm^{-2}. EWs are in units of eV.

3.3. *The Optical Spectrum*

We model the SOAR spectrum of NGC 7213, focusing on the Hα region assuming a power-law pseudo-continuum. We also include a series of Gaussian lines in emission to account for the narrow Hα line, [N II] $\lambda\lambda$6548, 6583, and [S II] $\lambda\lambda$6716, 6731. We assumed intensity ratios of 1:3 for [N II] $\lambda\lambda$6548, 6583 and 1:1 for [S II] $\lambda\lambda$6716, 6731. A broad Gaussian line is required by the data with a rest-frame wavelength consistent with that of Hα. The velocity shift and the widths of the narrow lines are linked. We added a couple of broad Gaussian emission lines red- and blueshifted with respect to the Hα rest-frame wavelength that are characteristic of DPB AGNs (see, e.g., M. Eracleous & J. P. Halpern 1994; J. S. Schimoia et al. 2017), with a velocity shift of $\sim\pm$(2200–2400) km s^{-1}. This model could not capture the full complexity of the data, as some residuals in excess could still be visible around the [N II] $\lambda\lambda$6548, 6583 and [S II] $\lambda\lambda$6716, 6731, which are most likely due to the presence of the broad blue wings associated with these lines (see, e.g., J. S. Schimoia et al. 2017). By adding broad blueshifted lines (~ -100 km s^{-1}) with respect to the narrow lines, the residuals flattened around these regions. Finally, we added two broad lines around $\sim$6475 and 6685 Å with an FWHM $\sim$ 900–1200 km s^{-1}, of unknown origin, which are required by the data. The spectrum and the best-fit model are shown in Figure 4. We note that the spectrum is not flux-calibrated. We also list the wavelengths and the FWHMs of each of the lines included in the model in Table 2. The results of this analysis are consistent with the findings of previous optical spectral studies of this source (S. Bianchi et al. 2008; J. S. Schimoia et al. 2017). The wavelengths of the narrow lines are redshifted with respect to the rest frame of the source by $\sim$80 km s^{-1} with an FWHM of $\sim$300 km s^{-1}. We obtained an FWHM for the symmetric broad Hα, thought to originate from the BLR, of 2020^{+4}_{-7} km s^{-1}.

The XRISM/Resolve spectrum of NGC 7213 revealed for the first time the presence of an asymmetric broad Fe Kα line. We modeled this line assuming a relativistically broadened disklike feature with an inner radius of $\sim 100\,R_g$ viewed at an inclination of $\sim$11°. This feature resembles the DPB emission line seen in Hα. In fact, various works have used a disklike profile or a variation of it to model optical DPB emission lines in AGNs (see, e.g., K. Chen & J. P. Halpern 1989; K. Chen et al. 1989; T. Storchi-Bergmann et al. 1993; M. Eracleous & J. P. Halpern 2003; I. V. Strateva et al. 2003; S. Bianchi et al. 2019, 2022; C. Ward et al. 2024, 2025). Such features are commonly modeled using disklike profiles and relatively flat emissivity indices ($q \sim 0$–2) that are smoothed with a Gaussian profile. This smoothing accounts for the local turbulence of the emitting gas, parameterized via a velocity dispersion ($\sigma_{\rm turb}$). Various authors have adopted a variety of emissivity profiles. However, the common feature in these works is that the emissivity index is flat in the inner regions and then drops in a faster way at larger radii. After subtracting the continuum as well as all the best-fit lines, except the broad red- and blueshifted lines, we modeled the double-peaked Hα with a relativistic DISKLINE model (A. C. Fabian et al. 1989) modified by a Gaussian smoothing to account for local turbulence. This model is chosen for consistency with the one adopted for the Fe Kα line, which facilitates the comparison between the two lines. The double-peaked profile and the best-fit model are shown in the left panel of Figure 5. We obtained

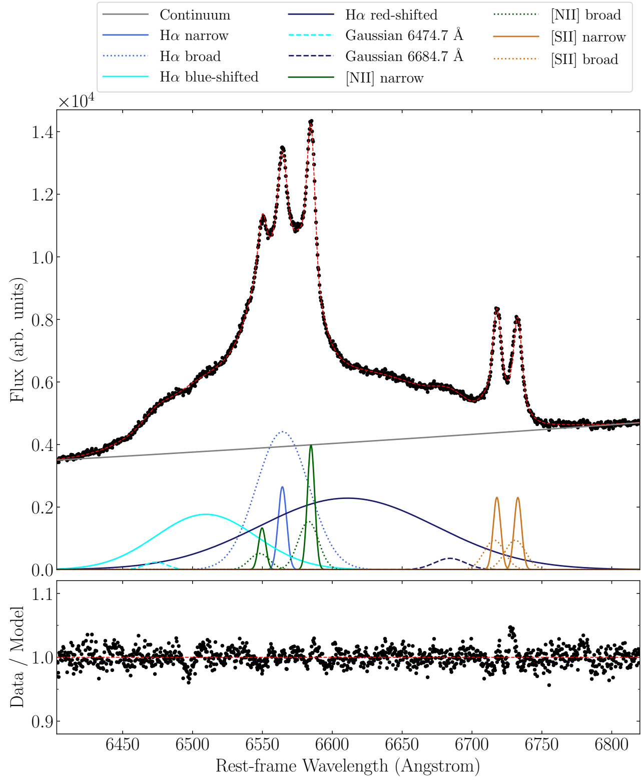

Figure 4. SOAR spectrum of NGC 7213 in the Hα region. We fit the data assuming a power-law continuum and a series of Gaussian emission lines to model the narrow Hα, a broad symmetric Hα line, two broad red-/blueshifted Hα lines, and narrow [N II] λλ6548, 6583 and [S II] λλ6716, 6731 lines. In addition, the data required broad and blueshifted [N II] λλ6548, 6583 and [S II] λλ6716, 6731, as well as a low-amplitude red-/blueshifted doublet at ∼6682 Å and ∼6472 Å, respectively, with an intermediate broadening of ∼900–1000 km s^{-1}.

Table 2

Best-fit Central Rest-frame Wavelengths (Assuming $z = 0.005839$), Wavelength Shifts with Respect to the Expected Value, and FWHMs of the Emission Lines Identified in the Hα Region of the NGC7213 SOAR Spectrum

Line	λ_0 (Å)	$\Delta\lambda$ (Å)	FWHM (km s^{-1})
Hα narrow	6564.3 ± 0.2	1.5 ± 0.2	325 ± 1
Hα broad	6564.4 ± 0.4	1.6 − 0.4	2020^{+4}_{-7}
Hα blue	6509.9 ± 0.2	−52.9 ± 0.2	3890^{+10}_{-20}
Hα red	$6610.9^{+0.2}_{-0.9}$	$48.1^{+0.2}_{-0.9}$	6760^{+10}_{-20}
Gaussian	$6474.7^{+0.3}_{-1.1}$	⋯	900^{+1}_{-6}
Gaussian	$6684.7^{+0.2}_{-0.9}$	⋯	1170^{+3}_{-4}
[N II] narrow	6549.79 ± 0.01	1.78 ± 0.01	280 ± 1
	6584.78 ± 0.01	1.78 ± 0.01	280^{tied}
[N II] broad	6547.92 ± 0.01	−0.08 ± 0.01	775 ± 5
	6582.92 ± 0.01	−0.08 ± 0.01	775^{tied}
[S II] narrow	6717.82 ± 0.01	1.8 ± 0.01	280^{tied}
	6732.83 ± 0.01	1.8 ± 0.01	280^{tied}
[S II] broad	6715.91 ± 0.01	−0.1 ± 0.01	775^{tied}
	6730.91 ± 0.01	−0.1 ± 0.01	775^{tied}

the best fit with an inclination $i = 18\overset{\circ}{.}8 \pm 0\overset{\circ}{.}3$, an inner radius $\log(R_{\mathrm{in}}/R_{\mathrm{g}}) = 2.32 \pm 0.05$, an outer radius $\log(R_{\mathrm{out}}/R_{\mathrm{g}}) = 3.16 \pm 0.05$, an emissivity index $q = 1.6^{+0.2}_{-0.3}$, and a local turbulent broadening $\sigma_{\mathrm{turb}} = 1420 \pm 50\,\mathrm{km\,s^{-1}}$. This turbulence requires a moderately high scale height, consistent with a flatter q value, as expected in low-/intermediate-accretion-rate sources (e.g., M. Elitzur et al. 2014).

4. Discussion

4.1. The Inner Edge of the Disk

In the right panel of Figure 5, we show the marginal and joint probability density plots of the inclination and inner radius obtained by modeling the broad asymmetric Fe Kα. The blue filled contours represent the posterior probability density obtained from the XRISM/Resolve Markov Chain Monte Carlo (MCMC) run. Within the main high-probability island, the two representations overlap closely, illustrating that the two measures are fully consistent in the region of interest. The faint elongated ridge that stretches toward higher inclinations and larger inner radii in the plane is a genuine mode explored by the sampler, but it carries very little posterior mass. Integrating the kernel density estimation gives a probability of $\sim 2 \times 10^{-3}$. Consistent with that, the smallest C-stat encountered anywhere along the ridge still lies at $\Delta C \simeq 13$ above the global minimum. We therefore regard the ridge as a statistically insignificant tail of the posterior and conduct all the quantitative inference with respect to the dominant peak.

We also show in this panel the best-fit inclination and inner radius derived from fitting the DPB Hα. The inner radii derived from both lines are fully consistent. The inclination derived from both lines agrees within $3\,\sigma$, although the Hα profile requires a slightly larger inclination. The emissivity index of the Fe Kα could not be constrained ($q > 0.1$) and is found to be broadly compatible with the standard value of $q = 3$; the emissivity index of the Hα is significantly flatter. We attempted to fit the broad Fe Kα by fixing all the parameters to the best-fit values obtained by modeling the Hα line. This worsens the fit by $\Delta C = 13$. This difference could have a physical origin. The double-peaked Balmer lines are thought to originate from the atmosphere of the accretion disk and/or the base of weak disk winds typically seen at low accretion rates (see, e.g., M. Eracleous et al. 2009, and references therein). It has been demonstrated that the DPB Balmer lines are preferentially produced in optically thin media ($\tau \lesssim 1$; see, e.g., N. Murray & J. Chiang 1997; H. M. L. G. Flohic et al. 2012; L. S. Chajet & P. B. Hall 2013). As the optical depth increases, the two peaks become closer and resemble a single-peaked emission line. The Fe Kα, instead, is thought to be produced at higher optical depths ($\tau \sim$ 1–2). This could indicate that the two lines are produced at the same radial distance from the central engine, though in different locations along the vertical extension of the disk. The Hα could be produced in the outer atmosphere and the Fe Kα deeper in the disk. In addition, the turbulent velocity of the Hα line ($\sigma_{\mathrm{turb}} \sim 1400\,\mathrm{km\,s^{-1}}$) also supports the idea that this line is produced in a rather turbulent medium, consistent with the outer atmosphere of the accretion disk. These physical considerations can consequently explain the marginal differences we see in inclination and emissivity index. This discrepancy could also arise from some model-dependent degeneracies between the various parameters of the model. However, given the quality of the data, the parameters of the two lines are consistent within $\sim 3\sigma$.

J. S. Schimoia et al. (2017) presented a monitoring campaign of the Hα emission line in this source over ∼2 yr.

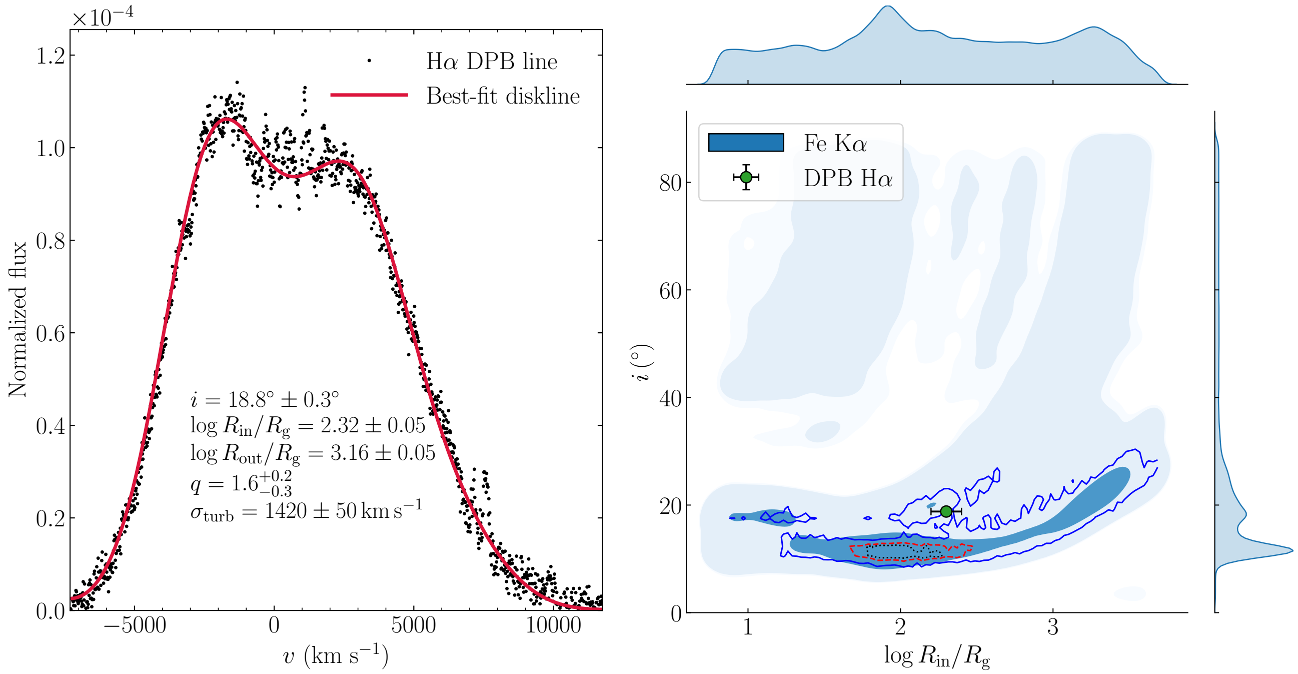

Figure 5. Left: the DPB Hα profile of NGC 7213 in velocity space modeled by a DISKLINE with an additional Gaussian smoothing. The negative/positive sign corresponds to blue-/redshift with respect to 6562.8 Å. Right: confidence contours of the disk inclination versus inner radius obtained by modeling the broad Fe Kα line in the XRISM/Resolve spectrum. The shaded regions enclose the 68%, 90%, and 95% posterior probability. The solid contours correspond to the contours derived from a grid of $\Delta C = 2.3$, 4.6, and 10 (black, red, and blue, respectively), which would correspond to 68%, 90%, and 99.5% confidence levels in the χ^2 approximation for two parameters of interest. The green circle shows the best fit obtained by modeling the DPB Hα profile on the left.

They showed that the profile of the double-peaked feature is variable and attributed this behavior to a precessing spiral arm in the accretion disk with a variable intensity. They also assumed a broken-power-law emissivity profile, where the inner emissivity index between $R_{\rm in}$ and a break radius ($R_{\rm q}$) is fixed at −0.2 and the outer emissivity index above $R_{\rm q}$ is fixed at 3. They found $R_{\rm in} = 300 \pm 60\,R_{\rm g}$, $R_{\rm q}$ varying between $1800\,R_{\rm g}$ and $3000\,R_{\rm g}$, and $i = 47° \pm 2°$. The inner and outer (break) disk radii found by J. S. Schimoia et al. (2017) are broadly consistent with the values we find in this work. The difference between their best-fit inclination and emissivity index and ours could be perceived as significant. This difference can be explained by degeneracies in the model used by J. S. Schimoia et al. (2017). In fact, the J. S. Schimoia et al. (2017) model has 10 parameters, as opposed to only four in our model. We performed a detailed comparison between the two models, confirming that the line profile presented in Figure 5 could be reproduced with the model by J. S. Schimoia et al. (2017) assuming $i = 47°$.

We note that an FWHM of the broad Fe Kα line is consistent with the FWHM of the symmetric core of the broad Hα line at $\sim2.7\sigma$. This does not completely rule out an origin of the broad Fe Kα that is consistent with the BLR similar to what is inferred in other sources (e.g., D. Bogensberger et al. 2025). However, the fact that a disk origin of the Fe Kα is statistically preferred, and the properties of the line being in agreement with the DPB Hα line, strongly suggest that the broad Fe Kα line may be originating from regions closer to the SMBH. In any case, it is likely that a wide range of radii, extending up to the optical BLR, could contribute to the broad Fe Kα line, given a certain emissivity profile. In addition, the BLR itself may also have a disklike shape or be closely associated with the accretion disk, as shown by the results from BLR reverberation mapping studies (e.g., F. Pozo Nuñez et al. 2013; A. Pancoast et al. 2014; C. J. Grier et al. 2017; P. R. Williams et al. 2020).

4.2. The Narrow Fe Kα Line

The XRISM/Resolve spectrum shows a clear narrow Fe Kα line with an FWHM = 650^{+240}_{-220} km s^{-1}. Assuming that the emitting gas follows an ordered rotation motion, the relation between the rotation velocity and the FWHM can be written as FWHM = $2v_{\rm rot}\sin i$. The distance of the emitting material can then be written as $R = GM_{\rm BH}/v_{\rm rot}^2$. For an inclination of 11°–19°, a BH mass of $0.2–2.4\times10^8\,M_\odot$, and also accounting for the uncertainty on the FWHM of the line, we obtain a radius of the narrow Fe Kα emitting region of $\sim(1.6–18)\times10^4\,R_{\rm g}$ ($\sim$0.01–2.1 pc). This large uncertainty is mainly driven by the uncertainty on the SMBH mass. We fitted the narrow Fe Kα with a ZFEKLOR model blurred with an RDBLUR (A. C. Fabian et al. 1989) kernel (equivalent to a DISKLINE model but accounting for the fact that Fe Kα is a doublet, which matters at such low velocities). We linked the inclination of this component to that of the broader Fe Kα line and left the inner edge free to vary. We obtained $R_{\rm in} = 1.4^{+2.0}_{-0.7}\times10^4\,R_{\rm g}$, consistent with our previous estimate, although with a smaller uncertainty. Considering the uncertainty on the BH mass, we obtain a physical radius of 0.01–0.4 pc.

Following the estimate by M. Nenkova et al. (2008), we calculate the dust sublimation radius as a function of the bolometric luminosity and the dust temperature, as follows:

$$R_{\rm sub} = 0.4\left(\frac{L_{\rm bol}}{10^{45}\ {\rm erg\ s^{-1}}}\right)^{1/2}\left(\frac{1500\ {\rm K}}{T_{\rm sub}}\right)^{2.6}\ {\rm pc}. \qquad (3)$$

For $L_{\rm bol} = 3\times10^{43}$ erg s^{-1} (see Section 3.1) and a dust sublimation temperature between 1000 and 1800 K, we obtain a dust sublimation distance of 0.04–0.2 pc, which is fully consistent with the distance of the Fe Kα emitting region. The presence of a narrow Fe Kα consistent with the dust sublimation radius could be an indication of a dusty torus. However, it is worth noting that the hard-X-ray spectrum of NGC 7213, from our analysis (Section 3.1) and a previous NuSTAR observation of the source (F. Ursini et al. 2015), does not show any indication of a Compton hump, which typically indicates reprocessing from cold material. This absence of a strong Compton hump is indicative of either a low column density of this material and/or of a small solid angle subtended by the torus. This also applies to the relativistically broadened Fe line. A detailed analysis of the broadband spectra of the source is deferred to a future publication.

We used Equation (5) of K. D. Murphy & T. Yaqoob (2009), which relates the Fe Kα line EW to the torus covering fraction ($f_{\rm cov} = \Delta\Omega/4\pi$) and the column density, which can be approximated as follows:

$$\mathrm{EW}_{\mathrm{Fe\,K}\alpha} \simeq 580 \times f_{\rm cov} \times \frac{N_{\rm H}}{10^{24}\ \mathrm{cm}^{-2}}\ \mathrm{eV}, \tag{4}$$

assuming a photon index $\Gamma = 1.75$. We estimate the covering fraction of the torus to be between 4% and 7% for $N_{\rm H} = 10^{24}\ \mathrm{cm}^{-2}$ and between 45% and 65% for $N_{\rm H} = 10^{23}\ \mathrm{cm}^{-2}$, given the line EW reported in Table 1. F. Ursini et al. (2015) estimated a torus column density $N_{\rm H} = 5^{+2.0}_{-1.6} \times 10^{23}\ \mathrm{cm}^{-2}$, which results in a covering fraction of ∼6%–20%, considering the uncertainties on the $\mathrm{EW}_{\mathrm{Fe\,K}\alpha}$ and $N_{\rm H}$. In addition, the reflection fraction (R) from a neutral optically thick slab can be derived from the Fe Kα EW as $R \simeq \mathrm{EW}_{\mathrm{Fe\,K}\alpha}/(150\ \mathrm{eV})$ (e.g., I. M. George & A. C. Fabian 1991). This results in $R = 0.17 \pm 0.12$. This value is consistent with the absence of a strong Compton hump in the NuSTAR spectrum and with the 3σ upper limit of $R < 0.2$ derived by F. Ursini et al. (2015).

The top panel of Figure 6 shows the 1D posterior distribution of the best-fitted line intensities of the narrow and the broad Fe Kα lines. For comparison, we also show the line intensity obtained by S. Bianchi et al. (2008), which is consistent with the sum of the intensities of the narrow and the broad lines. In fact, S. Bianchi et al. (2008) modeled the Fe Kα from Chandra/HETG assuming a single Gaussian line with an FWHM = 2400 km s^{-1}. The low spectral resolution of Chandra/HETG compared to XRISM/Resolve did not allow the authors to distinguish the two lines. Thus, the reported line intensity includes the contribution of both features.

In addition, we found only weak evidence of an Fe Kβ line. The 3σ upper limit on the Fe Kβ/Fe Kα ratio is 0.2. This is consistent with the 90% upper limit of 0.18 reported by S. Bianchi et al. (2008), which is also consistent with the expectation from neutral iron (see Section 3.3 of S. Molendi et al. 2003, for example).

We note that we also tested whether the asymmetry seen in the Fe Kα line could be caused by a Compton shoulder associated with the neutral emission from distant material, by testing reflection models. However, this test did not provide a satisfactory statistical and physical explanation of the data. On the one hand, the model left considerable residuals, mainly failing to explain the blue part of the Fe line. In addition, any significant Compton hump would require relatively large column densities, which would then imply a strong Compton hump that is in tension with the NuSTAR hard-X-ray spectra. In order to be able to account for this, large values of Fe abundance may be required (more than five times the solar abundance) to suppress the relative intensity of the Compton hump with respect to the Fe line. In addition, the fact that the properties inferred from modeling the Fe Kα line profile with disk emission agree with the properties inferred from the DPB

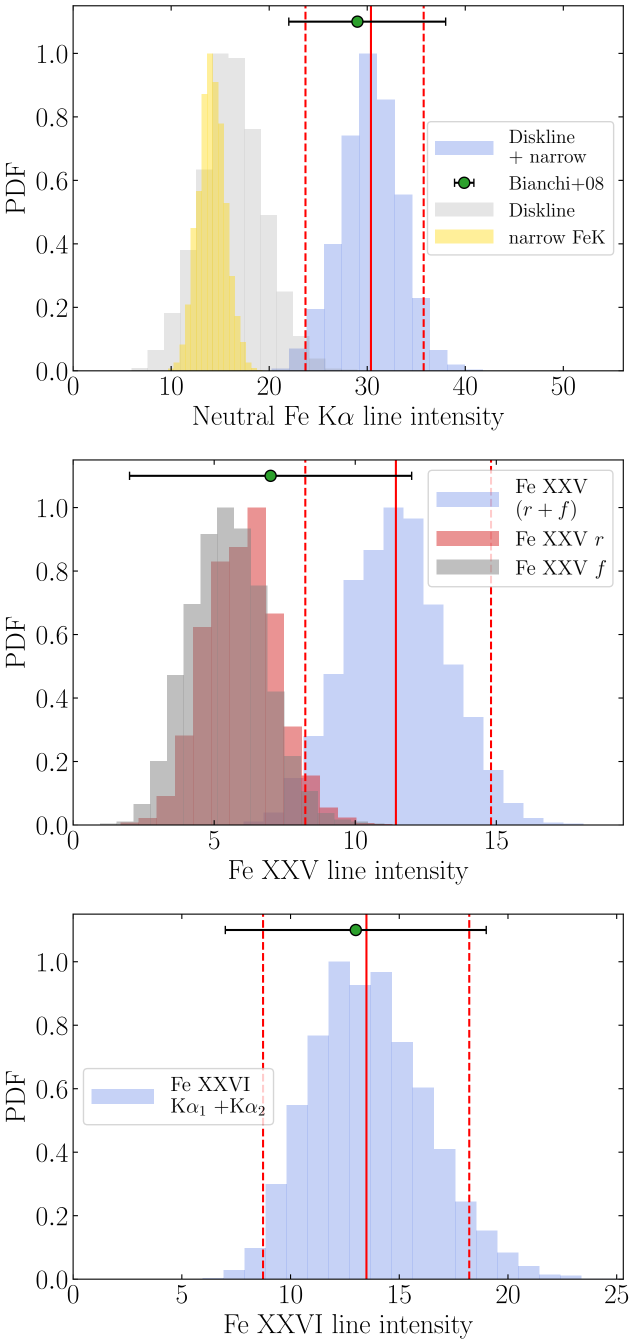

Figure 6. Posteriors of line fluxes obtained from the best fit to the XRISM/Resolve data (in units of 10^{-6} photon s^{-1} cm^{-2}). Top: line fluxes of the narrow DISKLINE Fe Kα and their sum (yellow, gray, and blue, respectively). Middle: line fluxes of the forbidden and resonant Fe XXV lines and their sum (gray, red, and blue, respectively). Bottom: line fluxes of the Fe XXVI K$\alpha_{1,2}$. The solid and dashed lines show the median and the 90% confidence range of the distributions, respectively. The green circles show the best-fit flux lines of the corresponding lines from Chandra/HETG reported by S. Bianchi et al. (2008).

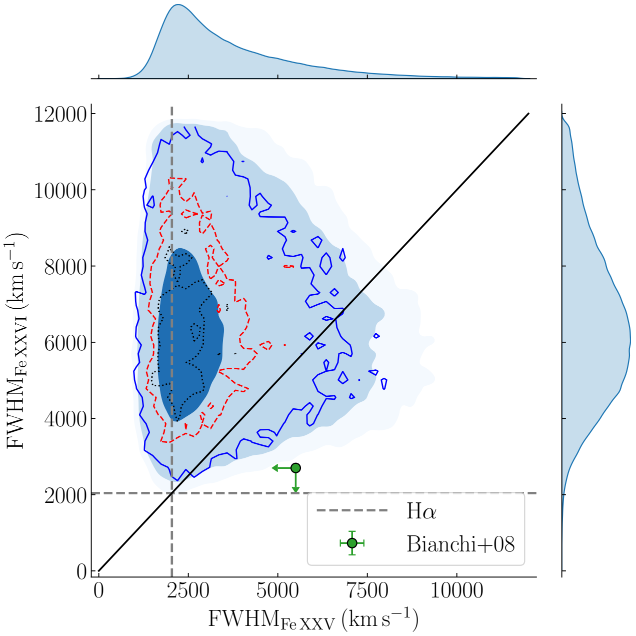

Figure 7. Confidence contours of the FWHMs of Fe XXV and Fe XXVI. The solid contours correspond to the contours derived from a grid of $\Delta C = 2.3$, 4.6, and 10 (black, red, and blue, respectively). The green circle shows the corresponding limits reported by S. Bianchi et al. (2008). The dashed gray lines show the FWHM of the symmetric broad Hα line. The solid black line shows the 1:1 relation.

Hα profile further support the hypothesis that the Fe Kα originates from the accretion disk.

4.3. *The Origin of the Fe XXV and Fe XXVI Lines*

We show in Section 3 that the XRISM/Resolve data required a significant broadening of the highly ionized Fe XXV and Fe XXVI emission lines. Figure 7 shows the 2D confidence contours of the FWHMs of the two lines. Fe XXVI requires a broader profile. However, the broadening of the two lines is consistent within 3 σ. The broadening of the Fe XXV lines is consistent with the symmetric core of the Hα profile (FWHM $= 2041^{+7}_{-6}$ km s^{-1}). Similar to the Fe Kα line, we estimated the distance of the emitting material from the BLR to the central SMBH. This results in a distance of the optical BLR of ∼8000–31,000 R_g (∼0.003–0.1 pc). These values agree with the variability timescales of ∼7–21 days of the symmetric broad Hα reported by J. S. Schimoia et al. (2017). If we assume that the broadening of the Fe XXV and Fe XXVI lines is due to the motion of the orbiting gas around the BH, the Fe XXV emitting region is consistent with the optical BLR, while the Fe XXVI line comes from closer to the SMBH, at a distance of ∼178–2500 R_g (∼0.2–30 $\times$ 10^{-3} pc). We show in Figure 8 the flux ratio of the forbidden over resonant Fe XXV lines. We find a median value of $0.9^{+0.6}_{-0.5}$, which cannot be conclusive about the origin of the lines. The testing of various photoionized versus collisionally ionized scenarios will be presented in a forthcoming publication (K. Murakami et al. 2025, in preparation).

S. Bianchi et al. (2008) modeled the Fe XXV and Fe XXVI emission lines in the Chandra/HETG spectrum using single Gaussian lines, consistent with the resonant line (6.7 keV) and the weighted mean of the Fe XXVI doublet (6.966 keV), respectively. Those authors report a hint of blueshift in these lines by 21^{+10}_{-16} eV (i.e., ∼1000 km s^{-1}). Given the fact that only a resonant Fe XXV line was detected, and the potential blueshift, the authors suggested that these lines could be originating from starburst activity in the host galaxy. Similar blueshift hints have been reported by F. Shi et al. (2022), who attributed this to hot winds from the accretion flow (see also F. Shi et al. 2024). However, our results do not show any shift in the line energies with respect to the rest frame of the source in the XRISM/Resolve spectra. This could indicate an intrinsic change in the state of the accretion flow as the source transitioned to higher fluxes (a factor of ∼2) or perhaps statistical limitations in the Chandra/HETG data. We show in the bottom two panels of Figure 6 the 1D distributions of the best-fitted intensities of the Fe XXV and Fe XXVI lines, respectively. We also show the corresponding intensities reported by S. Bianchi et al. (2008). For the Fe XXV, we show the individual histograms of the resonant and forbidden lines, as well as the sum of the two lines. Our estimate of the resonant line intensity is consistent with the one reported by S. Bianchi et al. (2008). We note that S. Bianchi et al. (2008) did not identify the presence of a forbidden line. This suggests that the properties of the lines may have changed, likely responding to the change in the flux of the source. As for the Fe XXVI intensity, presented in the bottom panel of Figure 6, we show the sum of the doublet from our analysis (assuming an intensity ratio of 2:1), which is consistent with the value reported by S. Bianchi et al. (2008).

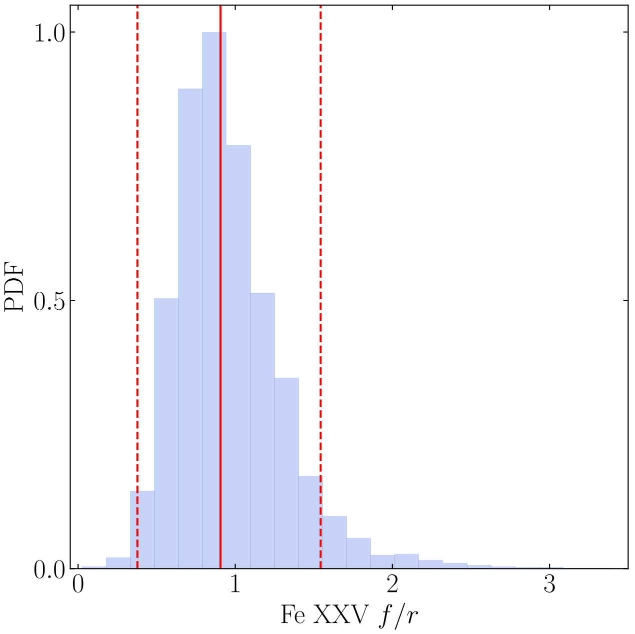

Figure 8. The posterior distribution of the Fe XXV forbidden-to-resonant line ratio. The red solid and dashed lines correspond to the median and 90% confidence region.

To further explore the possibility of long-term variability in Fe XXV and Fe XXVI, we show in Figure 7 the upper limits on the FWHMs of each of the lines reported by S. Bianchi et al. (2008). The upper limit on the Fe XXV FWHM of 5500 km s^{-1} is consistent with our estimate of the line width in XRISM/Resolve. However, the tight upper limit reported by S. Bianchi et al. (2008) on the FWHM of the Fe XXVI line (<2700 km s^{-1}) is lower by a factor of ∼3 compared to the value we find from the XRISM/Resolve spectrum. This further supports a scenario in which the highly ionized Fe lines are responding to the change in the intrinsic luminosity of the

AGN (twice that of the Chandra/HETG flux), favoring photoionization as the dominant excitation mechanism. Furthermore, the extreme broadening of the lines, notably the Fe XXVI FWHM exceeding 3800 km s^{-1} at the 90% confidence level, is a strong signature of an AGN origin. It is hard to produce a comparable broadening in the potential of the host galaxy. The detection of such broad lines in optical spectra is usually taken as a strong AGN signature. Finally, it is hard for processes other than AGN activity to produce photons that are energetic enough to ionize iron to Fe XXVI. In fact, the detection of even much lower ionization states of iron (i.e., [Fe X) is commonly used as an indicator of AGNs in dwarf galaxies (see, e.g., M. Molina et al. 2021; M. Reefe et al. 2023, and references therein). The combination of these three arguments makes a very strong case that these lines cannot come from the host galaxy. Further deep observations of the source at a different flux state will be essential to confirm the variability in these lines and identify their origin.

4.4. Additional Features

In addition to the features discussed earlier, the XRISM/Resolve spectrum shows the presence of two prominent emission lines at 6.45 and 6.75 keV of unknown origin. We modeled these features assuming Gaussian emission-line profiles with an unresolved width fixed at 100 km s^{-1} (comparable to the XRISM/Resolve energy resolution). We tested the hypothesis that these lines are produced by redshifted Fe XXV and Fe XXVI lines. To do so, we replaced the single Gaussian line with a quadruplet for Fe XXV with free intensities and with a doublet for Fe XXVI with a fixed intensity ratio of 2:1. Under these assumptions, we obtained redshift velocities that are broadly consistent for Fe XXV and Fe XXVI, estimated to be 8040^{+100}_{-70} km s^{-1} and 7730^{+80}_{-70} km s^{-1}, respectively. This model also requires the Fe XXV emission to be dominated by the intercombination line with forbidden and resonant lines consistent with zero. Investigating the origins of these lines and testing various scenarios goes beyond the scope of this Letter. Alternatively, if we assume that these two lines correspond to blueshifted low-ionization Fe Kα and resonant Fe XXV lines, this would result in a similar blueshift for both lines, of the order of -4000 km s^{-1}.

Furthermore, two narrow features could be identified redward of the Fe XXV and Fe XXVI lines, at ∼6.56 keV and ∼6.82 keV, respectively, albeit with a low statistical significance. We modeled these lines by fixing their rest-frame energies at the rest-frame energies of the Fe XXV resonant and Fe XXVI Kα_1 lines, assuming the same redshift for both lines. We also fixed the width of the lines at 100 km s^{-1}. The fit improved by only $\Delta C = -7$ for three additional free parameters. As discussed in Appendix C, these lines are significant with a 98% confidence level (∼2.3σ). We find a redshift of 4600^{+140}_{-110} km s^{-1}. If these lines are real, this may indicate the presence of a multiphase inflow in the source. Alternatively, if we assume that these lines are blueshifted low-ionization Fe Kα and resonant Fe XXV lines, we find a velocity of ∼–9000 km s^{-1} for the line at ∼6.56 keV and one of ∼–7000 km s^{-1} for the line at ∼6.82 keV. The best-fit model after adding these two lines and the lines at 6.45 and 6.75 keV, discussed previously, to the model is shown in Figure 9. We note that a hint of absorption at ∼6.52 keV appears in the data, though with low statistical significance. Deeper exposures may be required to confirm the presence of these features.

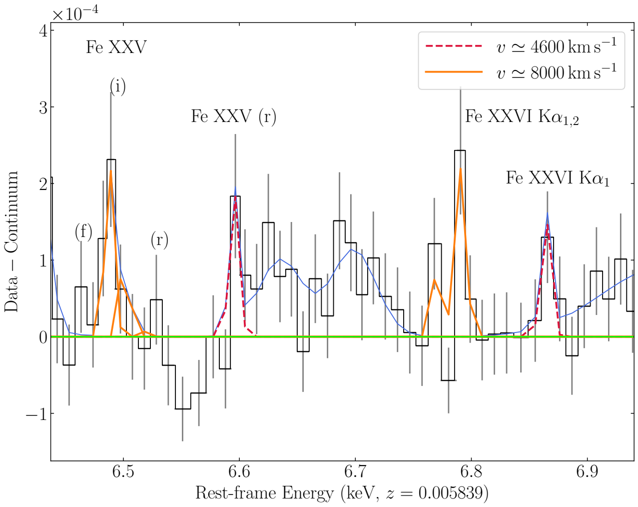

Figure 9. Residual of XRISM/Resolve data after subtracting the power-law continuum (in units of count s^{-1} cm^{-2} keV^{-1}), focusing on the observed 6.4–6.9 keV range. The blue line shows the total model fitting the emission lines in the residual. The orange solid and red dashed lines show the Gaussian lines assuming redshifted velocity of ∼8000 km s^{-1} and ∼4600 km s^{-1}, respectively, assuming Fe XXV and Fe XXVI.

4.5. A Self-consistent Picture

We attempt in this section to present a complete and self-consistent picture inferred from the modeling of the various features identified in the XRISM/Resolve data. We discuss two scenarios driven by the way the low-ionization Fe Kα can be modeled.

In the previous sections, we estimated the distances of the emitting regions for each line, assuming that the Fe features detected in the XRISM/Resolve spectrum are produced by photoionization and that their observed broadening arises from the orbital motion of the gas around the BH. In that scenario, we see a stratification of the line-emitting regions as follows: the broad Fe Kα and the DPB Hα lines are produced at $\sim 100\,R_{\mathrm{g}}$, the Fe XXVI lines are produced at $\sim 10^3\,R_{\mathrm{g}}$, the Fe XXV and the symmetric broad Hα lines are produced at $\sim 10^4\,R_{\mathrm{g}}$, and the narrow Fe K$\alpha$ line is produced at $\sim 10^5\,R_{\mathrm{g}}$. Figure 10 shows a schematic representation of the radial distribution of the various lines, where the ionizing X-ray and UV photons are generated within $\sim 100\,R_{\mathrm{g}}$ and the emission lines are distributed as discussed earlier. We note that this figure is not to scale and does not imply any assumptions on the geometry of the accretion flow below $100\,R_{\mathrm{g}}$ and/or the geometry of the X-ray corona. In this figure, the broad Fe Kα and the DPB Hα lines are produced at the same distance, in the inner part of the disk, which is connected to the region producing the broad symmetric core of the Hα line profile, at $R > 10^3\,R_{\mathrm{g}}$. The BLR emission is thought to be produced by gas with $\log(n_{\mathrm{e}}/\mathrm{cm}^{-3}) \gtrsim 10$, as estimated from the weakness of certain metastable and forbidden lines that become more prominent at lower gas density (see, e.g., K. Korista et al. 1997; M.-H. Ulrich et al. 1997; C. A. Negrete et al. 2012; A. Schnorr-Müller et al. 2016; P. Abolmasov & J. Poutanen 2017; M. Śniegowska et al. 2021, and references therein). The Hα profile emerging from the outer (Hα core) zone is single-

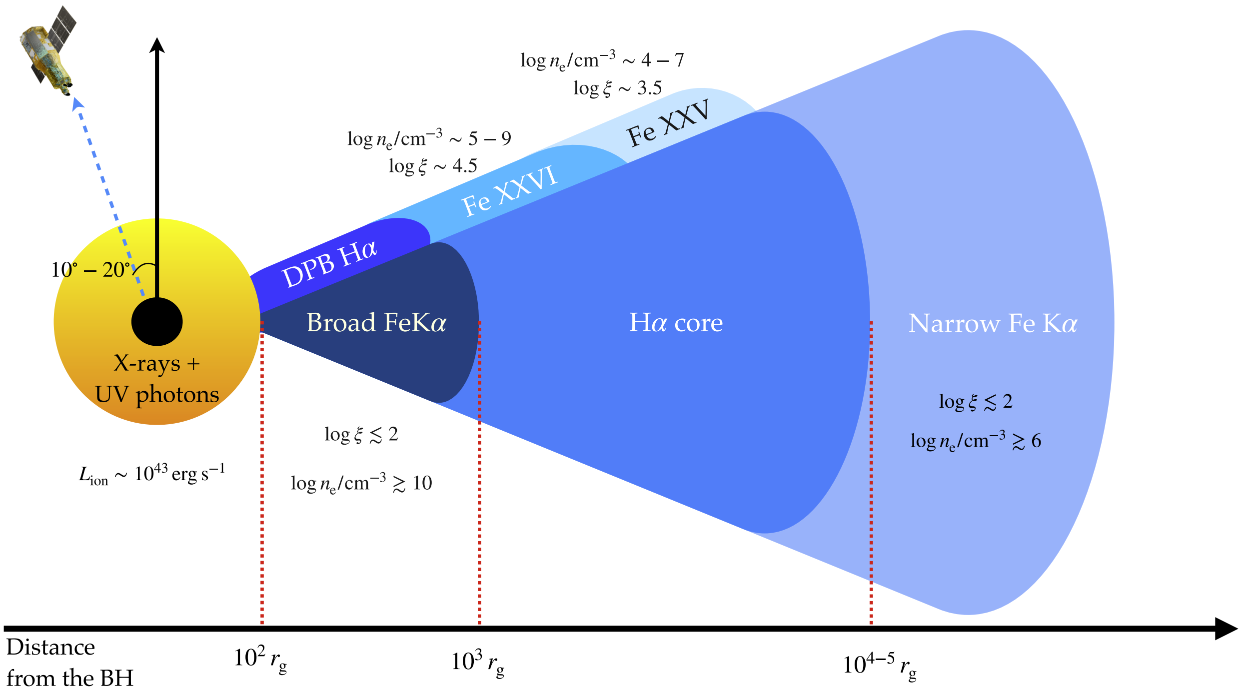

Figure 10. Schematic representation (not to scale), showing the radial stratification of the various emission lines reported in this work, under the assumption of photoionization by centrally concentrated X-ray and UV photons, and showing the broadening of the lines is caused by orbital motion around the SMBH.

peaked because of the large range in radii and a flat emissivity making up the core of the profile.

We use the definition of the ionization parameter to estimate approximately the electron density (n_e) needed to produce each of the Fe lines at the corresponding distance (R) from the ionizing source. The ionization parameter is defined as $\xi = L_{\mathrm{ion}}/n_e R^2$, where L_{ion} is the ionizing luminosity between 1 and 1000 Ry (0.0136–13.6 keV). We assume an ionizing luminosity of $\sim 10^{43}\,\mathrm{erg\,s^{-1}}$ and that the Fe Kα, Fe XXV, and Fe XXVI are produced at $\log(\xi/\mathrm{erg\,cm\,s^{-1}}) \lesssim 2$, ~ 3.5, and ~ 4.5, respectively.

The values of the ionization parameters correspond to the peaks of the line emissivities estimated using CLOUDY (C. M. Gunasekera et al. 2025). We obtain the following density estimates: $\log(n_e/\mathrm{cm}^{-3}) \gtrsim 10$, $\sim$5–9, $\sim$5–7, and $\sim$6 for the different Fe lines, according to their emitting radius. We note that these are approximate estimates, given the uncertainties on the mass and the FWHMs, and they are not intended to give exact measurements. While most of these numbers are reasonable, the value of $\log(n_e/\mathrm{cm}^{-3}) \sim 7$ is low compared to the density of the BLR emission. This suggests that the accretion flow itself is vertically stratified, with an upper atmosphere with a low density, which could be also outflowing (see, e.g., M. Elitzur et al. 2014).

In this scenario, the ionization is stratified in the vertical direction as well as in the radial direction, with the densest part concentrating around the midplane and in the inner region. The gas could then be distributed in a way that gives rise in the inner regions to Fe kα and Hα lines, although in different vertical layers, explaining the differences in the profiles of the two lines mentioned earlier. The outer region could then be emitting primarily Hα in the midplane, while the Fe XXV and Fe XXVI lines are emitted by the upper layer of the disk atmosphere, explaining the need for lower density and higher ionization parameters. We note that the proposed pictures will not hold under the assumption of a collisionally ionized gas producing the Fe XXV and Fe XXVI lines.

In the previous sections, we modeled separately the broad base and the narrow core of the low-ionization Fe Kα at 6.4 keV. However, these two features could also be modeled using a single DISKLINE feature extending from close to the BH up to $\sim 10^5\,R_g$, with an emissivity index of $q \sim 2$. A similar model has been found by D. Bogensberger et al. (2025) for Cen A. In our model, replacing GSmooth × zFeKlor$_{\mathrm{Fe\,K}\alpha}$ + diskline in Equation (2) with only DISKLINE, leaving the emissivity profile free to vary, results in an equally good fit ($C/\mathrm{dof} = 510/524$). The best-fit emissivity profile is $q = 2.1^{+0.1}_{-0.2}$, outer radius $\log(R_{\mathrm{out}}/R_g) = 5.2 \pm 0.5$, and inclination $i = 11^{+7}_{-2}$°. We obtained a best-fit inner radius of $80\,R_g$, with a 3σ upper limit of $R_{\mathrm{in}} < 1000\,R_g$. We show in Figure 11 the best fits to the line, assuming the sum of two lines with $q = 3$ and a single line with $q = 2.1$. This solution does not contradict the previous one consisting of two different lines. It presents a different perspective on the geometry of the system. The case of $q \sim 2$ is one of the rare emissivity profiles where the emission from both the inner part of the disk and the outer part can be detected in a single line profile. For lower-emissivity indices, the line profile is dominated by the narrow core (i.e., the outer regions), while for higher values, the inner radii (broad cores) dominate the emission, unless two lines with independent normalization are used. This behavior has been known and discussed for a few decades now (see, e.g., A. C. Fabian et al. 1989; A. Laor 1991). As pointed out by A. Laor (1991), a line with an emissivity profile of $q \sim 2$ is most sensitive to the outer edge. This is seen in our data by a well-constrained R_{out} and only an upper limit on R_{in}.

The two solutions strongly demonstrate that the contributions from both the inner and the outer radii to the line profile

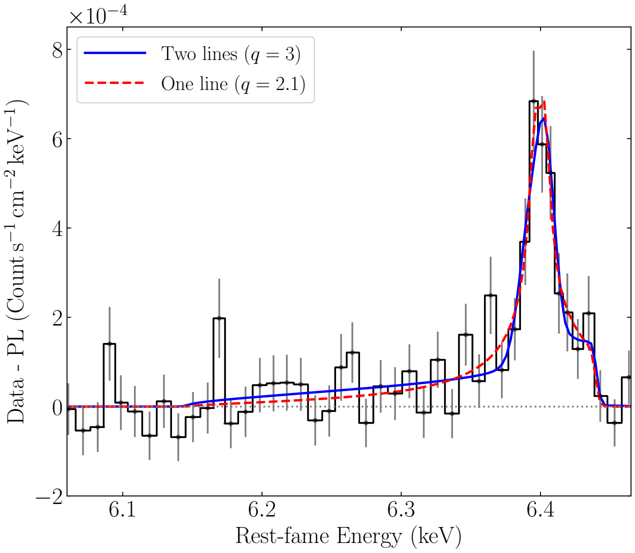

Figure 11. Best fit of the low-ionization Fe Kα, assuming two lines (a broad base and a narrow core) with $q = 3$ (solid blue line) and a single line with $q = 2.1$ (red dashed line). We show the data after subtracting the power law.

are needed to explain the observation. They both also result in consistent inner and outer radii and inclination. The flatter-than-3 emissivity profile can be an indication of a flaring/concave accretion disk, as shown by E. G. Blackman (1999), in their Figure 4. More recent general relativistic magnetohydrodynamic simulations also show that an emissivity profile consistent with $q \sim 2$ can be expected (e.g., B. E. Kinch et al. 2016, 2021). These simulations also consider an accretion disk with a thickness increasing with radius, and they also consider reprocessing in the upper layers of the disk, which can also help with flattening the emissivity profile. It could also be expected to have a broken-power-law emissivity profile. However, the current data quality does not allow for testing such a complicated model. Further observation of this source, as well as other AGNs, would be of great importance for studying their line profiles and better understanding the structure of the reprocessing material.

4.6. NGC 7213 as an Intermediate Case between LLAGNs and Seyferts

The XRISM/Resolve results place NGC 7213 squarely between the torus-starved LINER M81* ($\lambda_{\rm Edd} \simeq 10^{-5}$; L. C. Ho et al. 1996), where only a distant Fe Kα core is detected (J. M. Miller et al. 2025), and the archetypal Seyfert NGC 4151 ($\lambda_{\rm Edd} \simeq 0.02$; P. Lubiński et al. 2016), which shows Fe Kα emission from the torus down to $\sim$100 R_g (Xrism Collaboration et al. 2024). In NGC 7213, a narrow core at $R \sim (0.7–3) \times 10^4 R_g$ coexists with a DISKLINE at $R \sim 40–300 R_g$, implying a radially stratified flow: an inner low-luminosity annulus of a thin disk plus an outer region that resembles the torus/BLR complex of more luminous Seyferts. The narrow Fe Kα radius in NGC 7213 matches the dust sublimation radius, yet its weak Compton hump and low Fe Kβ/Fe Kα ratio echo the properties of M81*. In addition, the EW of the narrow Fe Kα in NGC 7213 (EW = 32 ± 6 eV) is similar to that found in M81* (EW = 37^{+7}_{-6} eV; J. M. Miller et al. 2025). We applied Equation (4) to M81*, using the best-fit photon index ($\Gamma = 2$) and column density ($N_{\rm H} = 1.6 \times 10^{24}$ cm^{-2}) reported by J. M. Miller et al. (2025). We find a torus covering fraction of 5%. As for NGC 4151, we estimate an EW of the distant Fe Kα based on the best-fit parameters reported by Xrism Collaboration et al. (2024) to be $\sim$50 eV. For the best-fit photon index and column density ($\Gamma = 1.7$ and $N_{\rm H} = 2 \times 10^{23}$ cm^{-2}, as listed in Table 1 of Xrism Collaboration et al. 2024), we find a torus covering fraction of 40%. Thus, the torus covering fraction of NGC 7213 lies between that of M81* and NGC 4151. We therefore view NGC 7213 as occupying an intermediate-accretion regime, in which the BLR and inner disk persist while the cold optically thick torus may have already begun to dissipate. This further supports earlier predictions that the BLR and torus should disappear at low accretion rates (see, e.g., F. Nicastro 2000; A. Laor 2003; M. Elitzur & L. C. Ho 2009).

5. Conclusions

We have presented the first XRISM/Resolve observation of NGC 7213, an intermediate-/low-accretion-rate AGN ($\lambda_{\rm Edd} \sim$ 0.1%–1%). The unprecedented spectral resolution of Resolve has enabled us to resolve the complex iron structure of this source, revealing radial stratification spanning nearly 4 orders of magnitude in distance from the central BH.

Our key findings are as follows:

1. *Multicomponent* Fe Kα *emission*. The neutral Fe Kα line consists of a narrow core (FWHM = 650 km s^{-1}) originating from distant Compton-thin material, consistent with the dust sublimation radius. Superimposed on this is a broader asymmetric component best described by relativistic disk emission from $R_{\rm in} \sim 100 R_g$, viewed at a low inclination $i \sim 11°$. The broad Fe Kα profile mirrors the DPB Hα emission observed in our simultaneous SOAR spectrum.
2. *Highly ionized iron emission*. We detect resolved Fe XXV (forbidden and resonant) and Fe XXVI K$\alpha_{1,2}$ emission lines with FWHMs $\sim$2500 km s^{-1} and 6000 km s^{-1}, respectively. Assuming Keplerian broadening, these lines originate at intermediate radii between the inner disk and optical BLR.
3. *Radial and vertical stratification*. Under a photoionization scenario, the observed line properties suggest both radial stratification and vertical stratification, with high-ionization lines requiring lower densities ($\log(n_e/{\rm cm}^{-3}) \sim$ 5–7) than expected for the BLR midplane ($\log(n_e/{\rm cm}^{-3}) > 10$), indicating emission from an extended disk atmosphere.
4. *Weak torus signature*. The narrow Fe Kα has a low EW (EW = 32 ± 6 eV), and the hard-X-ray spectrum shows no significant Compton hump. These observations point to a low-covering-fraction ($f_{\rm cov} \sim$ 6%–20%) and/or low-column-density (a few times 10^{23} cm^{-2}) torus, consistent with theoretical predictions for torus dissipation at low accretion rates.

Our results establish NGC 7213 as occupying an intermediate-accretion regime between classical Seyferts and LLAGNs. NGC 7213 retains an inner accretion disk and functioning BLR, similar to higher-luminosity Seyferts. However, its torus shows clear signs of a low covering fraction, similar to LLAGNs. This supports theoretical predictions for structural evolution with a declining accretion rate and places the critical $\lambda_{\rm Edd} \sim 0.01$ threshold where previous studies suggested the dusty torus begins to disappear.

The detection of both disklike Fe Kα emission and highly ionized Fe XXV and Fe XXVI lines bridging the gap between the inner disk and BLR provides the first X-ray spectroscopic evidence, to our knowledge, for a continuous, radially stratified flow in an intermediate-accretion source. This suggests that the disk, disk wind, BLR, and torus may form a continuum rather than discrete regions.

Several aspects of our findings warrant further investigation. While our interpretation assumes photoionization drives the Fe XXV and Fe XXVI emission, collisional ionization in hot winds or shocks remains viable, and the Fe XXV forbidden-to-resonant ratio ($0.9^{+0.6}_{-0.5}$) is not conclusive. We detect additional emission lines at 6.45 and 6.75 keV (each $\sim$3.3σ significant), plus weaker features at 6.56 and 6.82 keV ($\sim$22.3σ), which could indicate either inflow or outflow, depending on the interpretations of the lines. The apparent broadening of Fe XXVI compared to the Chandra/HETG upper limits suggests a potential response to the factor-of-2 luminosity increase, favoring photoionization, though confirmation requires multiepoch monitoring. Future tests include: (1) coordinated optical–X-ray monitoring, to reveal correlated Fe Kα/Hα variability from disk structures and constrain vertical stratification through disparate timescales; (2) reverberation mapping, to confirm photoionization and measure distances independently; (3) XRISM observations of additional sources with $\lambda_{\rm Edd} \lesssim 10^{-2}$, to establish whether NGC 7213's apparent stratification and torus properties represent universal evolution or source-specific geometry; and (4) deeper XRISM exposures, to confirm weak features, improve Fe XXV diagnostics, and enable time-resolved spectroscopy.

Our results may have broad implications for AGN physics. The detection of highly ionized iron at intermediate radii from a low-density atmosphere supports thermally driven disk wind models, where the BLR arises from the failed wind or disk atmosphere, with required density stratification consistent with such scenarios. The persistence of disk emission down to $\sim$100 $R_{\rm g}$ at $\lambda_{\rm Edd} \sim$ 0.1%–1% constrains radiatively inefficient flow models. If a hot inner flow exists, its truncation radius must lie even closer in, or the disk remains thin throughout. The low covering fraction and weak Compton hump, intermediate between M81* and NGC 4151, support gradual torus dissipation with a decreasing accretion rate, with implications for AGN unification at low luminosities. In summary, XRISM/Resolve has revealed NGC 7213 as a radially and vertically stratified system bridging LINERs and Seyferts. Future multiwavelength campaigns targeting similar intermediate-accretion sources will be essential for understanding the transition between radiatively efficient and inefficient modes and mapping the innermost AGN structure across the full range of BH feeding rates.

Acknowledgments

We would like to thank the anonymous referee for the prompt and insightful feedback that helped improve the analysis. We would like to thank the SOC members of XRISM, NuSTAR, and XMM-Newton for coordinating the observations, as well as Anna Ogorzalek and the XRISM helpdesk colleagues who assisted in the early stages of the data reduction. E.K. would like to thank Erin Kara and Dan Wilkins for fruitful discussions.

F.N., E.P., A.L., F.P., R.S., M.D., A.C., G.L., C.P., E.N., F. T., G.M., S.B., C.V., and A.M. acknowledge financial support from the Bando Ricerca Fondamentale INAF 2023, Large Program 1.05.23.01.06 (“The XRISM-to-XIFU (X2X) Agreement and Beyond: entering a new Era of High Resolution X-Ray Spectroscopy”). F.T., F.N., M.L., M.D., and M.C. acknowledge financial support from PRIN MUR 2022 DRAGON 2022K9N5B4. E.B. acknowledges financial support from INAF under the Large grant 2022 “The metal circle: a new sharp view of the baryon cycle up to Cosmic Dawn with the latest generation IFU facilities,” the GO grant “A JWST/MIRI MIRACLE: Mid-IR Activity of Circumnuclear Line Emission,” and the “Ricerca Fondamentale 2024” program (minigrant 1.05.24.07.01). V.E.G. acknowledges funding under NASA contract 80NSSC24K1403. F.P. acknowledges financial support from the Bando Ricerca Fondamentale INAF 2023. C.P. acknowledges funding from PRIN MUR 2022 SEAWIND 2022Y2T94C, supported by European Union—Next Generation EU, Mission 4, Component 1, CUP C53D23001330006. G.P. acknowledges support from the European Research Council (ERC) under the European Union’s Horizon 2020 research and innovation program HotMilk (grant agreement No. 865637), support from Bando per il Finanziamento della Ricerca Fondamentale 2022 dell’Istituto Nazionale di Astrofisica (INAF): GO Large program, and from the Framework per l’Attrazione e il Rafforzamento delle Eccellenze (FARE) per la ricerca in Italia (R20L5S39T9). R.S. acknowledges funding from the CAS-ANID grant No. CAS220016.

This research has made use of data and/or software provided by the High Energy Astrophysics Science Archive Research Center (HEASARC), which is a service of the Astrophysics Science Division at NASA/GSFC and the High Energy Astrophysics Division of the Smithsonian Astrophysical Observatory. This research has made use of pandas (W. McKinney 2010, 2011) and Astropy, a community-developed core Python package for Astronomy (Astropy Collaboration et al. 2018, 2013). This research has made use of XSPEC (K. A. Arnaud 1996). This research has made use of SciPy (P. Virtanen et al. 2020), matplotlib, a Python library for publication-quality graphics (J. D. Hunter 2007), and NumPy (C. R. Harris et al. 2020). This research is based on observations obtained with XRISM, a JAXA/NASA collaborative mission, with ESA participation, and XMM-Newton, an ESA science mission with instruments and contributions directly funded by ESA Member States and NASA. The NuSTAR mission is a project led by the California Institute of Technology, managed by the Jet Propulsion Laboratory, and funded by the National Aeronautics and Space Administration. Data analysis was performed using the NuSTAR Data Analysis Software (NuSTARDAS), jointly developed by the ASI Science Data Center (SSDC, Italy) and the California Institute of Technology (USA).

Facilities: XRISM, XMM, NuSTAR, SOAR.

Appendix A
The Effect of the COR

We explore in this section the effect of the COR on our results. We extracted XRISM/Resolve spectra assuming no COR and COR > 6, 8, and 10. The net exposure time decreases for 111 ks for no COR to 52 ks for COR > 10. We fitted each of the spectra with the model presented in

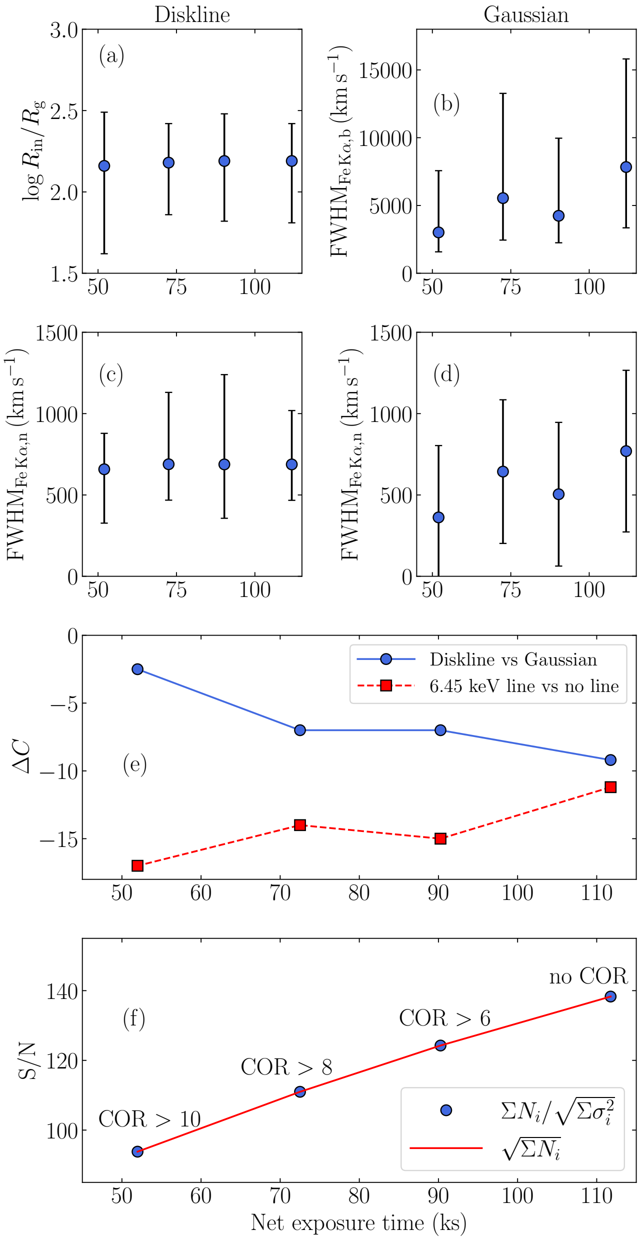

Figure 12. Effect of the COR on the best-fit parameters. The left and right panels correspond to the best-fit parameters obtained for modeling the broad Fe Kα with a DISKLINE and a symmetric Gaussian-broadened line, respectively. Panels (a) and (c) show the inner radius for the DISKLINE and the FWHM of the narrow Fe Kα, respectively. Panels (b) and (d) show the FWHM of the broad and narrow Fe Kα lines, respectively. Panel (e) shows the improvement in fit statistics for a DISKLINE with respect to a Gaussian-broadened line (blue circles) and the improvement obtained by including the emission line at 6.45 keV (red squares) for different COR values. Panel (f) shows the S/N of the full spectrum in the 5.5–7.5 keV range (see the text for details).

Equation (1), which models the broad low-ionization Fe Kα line with a Gaussian-broadened line and with a DISKLINE. We show in Figure 12 the best-fit parameters as a function of the net exposure time. For the DISKLINE model, we show the inner radius and FWHM of the narrow Fe Kα (panels (a) and (c), respectively). For the Gaussian-broadened model, we show the FWHMs of the broad and narrow Fe Kα (panels (b) and (d), respectively). This figure shows that the properties of the Fe Kα lines are consistent for the different COR choices. In panel (e), we show the improvement of the fit (ΔC) obtained by using DISKLINE instead of a symmetric broadening (blue circles). The fit improvement due to the DISKLINE increases for larger exposures. We note that this is not a measure of whether the broad line exists or not. It is to test the ability to identify an asymmetric versus a symmetric line profile. We also show the improvement of the fit when a Gaussian line at 6.45 keV is included (red squares). This has an opposite trend with respect to the broad line. We believe that this opposite behavior is caused by the effect of the COR. For the broad line, the distinction between an asymmetric and a symmetric line requires a higher number of counts (and thus a larger overall S/N). We show the overall S/N in the 5.5–7.5 keV range in panel (f). We estimate the S/N as follows:

$$\mathrm{S/N} = \frac{\sum_i N_i}{\sqrt{\sum_i \sigma_i^2}}, \qquad \text{(A1)}$$

where N_i and σ_i are the number of counts and their corresponding uncertainty in each channel. As panel (f) shows, this is equivalent to $\mathrm{S/N} = \sqrt{\sum_i N_i}$, which is expected for Poisson statistics. However, in the case of the narrow line, excluding low-COR intervals enables a better detection of the weak features. In any case, even for the case of no COR filtering, the improvement of the fit caused by the addition of the narrow line is still significantly high ($\Delta C < -10$). This exercise justifies our choice of COR > 6, as an intermediate case where the loss in exposure is only ∼10%.

Appendix B
MCMC Convergence

Standard convergence diagnostics (Geweke z-scores $|z| < 0.3$, stable cumulative means, and variances) together with an effective sample size of $\sim 7 \times 10^4$ confirm that the retained samples provide an adequate representation of the target posterior. For all parameter-space visualizations, we plot the raw post-burn chain, whose point density is already proportional to the posterior. Quantities derived from the posterior (such as synthetic line profiles or marginal percentiles) are computed from a thinned subset limited to samples with $\Delta C \leqslant 10$. Each retained sample has an associated C-stat stored by XSPEC; we restore the exact posterior measure by assigning the weight $w_k = \exp[-0.5(C_k - C_{\rm min})]$ and renormalizing so that $\sum_k w_k = 1$. This weighting reproduces the full posterior integrals at negligible computational cost. Weighted percentiles of the model flux in every energy bin yield the median spectrum and its 68% and 95% credibility bands (right panel of Figure 3). The procedure automatically propagates the full parameter covariance without additional error analysis. Marginal medians and 90% credibility limits are reported in Table 1 and defined in the same way.

Appendix C
Line Significance

As is already known, it is not straightforward to assess the significance of a spectral component using C-stat. For that reason, we ran a set of simulations using the same response files and exposure time (90 ks) as the observations studied in this work.

C.1. *DISKLINE versus Symmetric Line*

As discussed in Section 3.2, the best fit improves by $\Delta C = C_{\rm diskline} - C_{\rm symmetric} = -7$ using an asymmetric DISKLINE compared to a symmetric Gaussian-broadened emission line. We used the best-fit model, in which the broad low-ionization Fe Kα is modeled with GSMOOTH × ZFEKLOR. Using the XSPEC command FAKEIT, we produced 1000 simulated spectra, which we fitted using the same model and also using DISKLINE. In the latter case, we restricted the parameter space to $R_{\rm in} < 500\,R_{\rm g}$ and $i < 20°$, to be consistent with the best-fit results, favoring also an asymmetric profile. Allowing $R_{\rm in}$ to reach larger values would result in more symmetric line profiles. We found that when simulating with a symmetric line, an asymmetric model could provide a better fit with $\Delta C \leqslant -7$ in only nine cases out of 1000. This is equivalent to a confidence level of 99.1% (equivalent to 2.6σ) of the asymmetric model not being produced by chance due to the noise in the data. We also repeated the same exercise by simulating an asymmetric line while fitting with both an asymmetric and a symmetric model. In this case, we find that the median of the ΔC is −7.6, which is consistent with the value of −7 that we found from the observations. In addition, we found that when simulating an asymmetric line, a symmetric line could be preferred ($\Delta C > 0$) in 5% of the cases.

C.2. *Gaussian Lines at 6.45 and 6.75 keV*

To estimate the significance of the emission lines at 6.45 and 6.75 keV, we also ran a set of 1000 simulations assuming the best-fit model presented in Section 3.2, where we set the normalizations of these two lines to be zero. Then we fitted the simulated spectra using a model with normalizations fixed at zero, then by letting the normalizations free to vary. In this case, we can assess the probability of finding those lines due to noise in the data. We find that, for both lines, there is only a one-thousandth case where $\Delta C = C_{\rm line} - C_{\rm no\ line}$ is smaller than the values we found from the observations (see Table 1). This indicates that the presence of these lines is significant at 99.9% (∼3.3σ).

C.3. *Weak Gaussian Lines at 6.56 and 6.82 keV*

We repeated the same exercise to assess the significance of the lines discussed in Section 4.4 at ∼6.56 and 6.82 keV (found with $\Delta C = C_{\rm line} - C_{\rm no\ line} = -7$). Similar to the previous section, we ran simulations assuming the normalizations are zero. We fitted with normalizations fixed at zero and free to vary. In this case, we find that these lines could be found in the simulated spectra with $\Delta C < -7$ in 20 simulations out of 1000. This indicates a confidence level of 98% (∼2.3σ).

ORCID iDs

E. Kammoun https://orcid.org/0000-0002-0273-218X
T. Kawamuro https://orcid.org/0000-0002-6808-2052
S. Bianchi https://orcid.org/0000-0002-4622-4240
F. Nicastro https://orcid.org/0000-0002-6896-1364
A. Luminari https://orcid.org/0000-0002-1035-8618
E. Aydi https://orcid.org/0000-0001-8525-3442
M. Eracleous https://orcid.org/0000-0002-3719-940X
O. K. Adegoke https://orcid.org/0000-0002-5966-4210
E. Bertola https://orcid.org/0000-0001-5487-2830
P. G. Boorman https://orcid.org/0000-0001-9379-4716
V. Braito https://orcid.org/0000-0002-2629-4989
G. Bruni https://orcid.org/0000-0002-5182-6289
A. Comastri https://orcid.org/0000-0003-3451-9970
P. Condò https://orcid.org/0009-0005-9183-8662
M. Dadina https://orcid.org/0000-0002-7858-7564
T. Enoto https://orcid.org/0000-0003-1244-3100
J. A. García https://orcid.org/0000-0003-3828-2448
V. E. Gianolli https://orcid.org/0000-0002-9719-8740
F. A. Harrison https://orcid.org/0000-0002-4226-8959
G. Lanzuisi https://orcid.org/0000-0001-9094-0984
M. Laurenti https://orcid.org/0000-0001-5762-6360
A. Marinucci https://orcid.org/0000-0002-2055-4946
G. Mastroserio https://orcid.org/0000-0003-4216-7936
G. Matt https://orcid.org/0000-0002-2152-0916
G. Matzeu https://orcid.org/0000-0003-1994-5322
R. Middei https://orcid.org/0000-0001-9815-9092
E. Nardini https://orcid.org/0000-0001-9226-8992
H. Noda https://orcid.org/0000-0001-6020-517X
F. Panessa https://orcid.org/0000-0003-0543-3617
E. Piconcelli https://orcid.org/0000-0001-9095-2782
C. Pinto https://orcid.org/0000-0003-2532-7379
J. M. Piotrowska https://orcid.org/0000-0003-1661-2338
G. Ponti https://orcid.org/0000-0003-0293-3608
C. Ricci https://orcid.org/0000-0001-5231-2645
R. Ricci https://orcid.org/0000-0003-4631-1528
R. Serafinelli https://orcid.org/0000-0003-1200-5071
F. Shi https://orcid.org/0000-0003-3922-5007
D. Stern https://orcid.org/0000-0003-2686-9241
Y. Terashima https://orcid.org/0000-0003-1780-5481
R. Tomaru https://orcid.org/0000-0002-6797-2539
F. Tombesi https://orcid.org/0000-0002-6562-8654
A. Tortosa https://orcid.org/0000-0003-3450-6483
Y. Ueda https://orcid.org/0000-0001-7821-6715
F. Ursini https://orcid.org/0000-0001-9442-7897
C. Vignali https://orcid.org/0000-0002-8853-9611
S. Yamada https://orcid.org/0000-0002-9754-3081
S. Yamada https://orcid.org/0000-0003-4808-893X

References

Abolmasov, P., & Poutanen, J. 2017, MNRAS, 464, 152
Andonie, C., Bauer, F. E., Carraro, R., et al. 2022, A&A, 664, A46
Arnaud, K. A. 1996, in ASP Conf. Ser. 101, Astronomical Data Analysis Software and Systems V, ed. G. H. Jacoby & J. Barnes (San Francisco, CA: ASP), 17
Astropy Collaboration, Price-Whelan, A. M., Sipőcz, E. J., et al. 2018, AJ, 156, 123
Astropy Collaboration, Robitaille, T. P., Tollerud, E. J., et al. 2013, A&A, 558, A33
Baskin, A., & Laor, A. 2018, MNRAS, 474, 1970
Bell, M. E., Tzioumis, T., Uttley, P., et al. 2011, MNRAS, 411, 402
Bianchi, S., Antonucci, R., Capetti, A., et al. 2019, MNRAS, 488, L1
Bianchi, S., Chiaberge, M., Laor, A., et al. 2022, MNRAS, 516, 5775
Bianchi, S., La Franca, F., Matt, G., et al. 2008, MNRAS, 389, L52
Blackman, E. G. 1999, MNRAS, 306, L25
Blandford, R. D., & McKee, C. F. 1982, ApJ, 255, 419
Bogensberger, D., Nakatani, Y., Yaqoob, T., et al. 2025, PASJ, 77, S209
Cash, W. 1979, ApJ, 228, 939
Chajet, L. S., & Hall, P. B. 2013, MNRAS, 429, 3214
Chen, K., & Halpern, J. P. 1989, ApJ, 344, 115
Chen, K., Halpern, J. P., & Filippenko, A. V. 1989, ApJ, 339, 742
Clemens, J. C., Crain, J. A., & Anderson, R. 2004, Proc. SPIE, 5492, 331
Collin-Souffrin, S. 1987, A&A, 179, 60
Collin-Souffrin, S., Dyson, J. E., McDowell, J. C., & Perry, J. J. 1988, MNRAS, 232, 539

Duras, F., Bongiorno, A., Ricci, F., et al. 2020, A&A, 636, A73

Elitzur, M., & Ho, L. C. 2009, ApJL, 701, L91

Elitzur, M., Ho, L. C., & Trump, J. R. 2014, MNRAS, 438, 3340

Emmanoulopoulos, D., Papadakis, I. E., McHardy, I. M., et al. 2012, MNRAS, 424, 1327

Emmering, R. T., Blandford, R. D., & Shlosman, I. 1992, ApJ, 385, 460

Eracleous, M., & Halpern, J. P. 1994, ApJS, 90, 1

Eracleous, M., & Halpern, J. P. 2003, ApJ, 599, 886

Eracleous, M., Lewis, K. T., & Flohic, H. M. L. G. 2009, NewAR, 53, 133

Fabian, A. C., Rees, M. J., Stella, L., & White, N. E. 1989, MNRAS, 238, 729

Flohic, H. M. L. G., Eracleous, M., & Bogdanović, T. 2012, ApJ, 753, 133

Gandhi, P., Hönig, S. F., & Kishimoto, M. 2015, ApJ, 812, 113

George, I. M., & Fabian, A. C. 1991, MNRAS, 249, 352

Gezari, S., Halpern, J. P., & Eracleous, M. 2007, ApJS, 169, 167

GRAVITY Collaboration, Amorim, A., Bourdarot, G., et al. 2024, A&A, 684, A167

Grefenstette, B., Bhargava, Y., Fuerst, F., et al., 2025 NuSTAR/nustar-gen-utils: The One with Zenodo, v0.7, Zenodo, doi:10.5281/zenodo.14969199

Grier, C. J., Pancoast, A., Barth, A. J., et al. 2017, ApJ, 849, 146

Gunasekera, C. M., van Hoof, P. A. M., Dehghanian, M., et al. 2025, arXiv:2508.01102

Harris, C. R., Millman, K. J., van der Walt, S. J., et al. 2020, Natur, 585, 357

HI4PI Collaboration, Ben Bekhti, N., Flöer, L., et al. 2016, A&A, 594, A116

Ho, L. C., Filippenko, A. V., & Sargent, W. L. W. 1996, ApJ, 462, 183

Hölzer, G., Fritsch, M., Deutsch, M., Härtwig, J., & Förster, E. 1997, PhRvA, 56, 4554

Hunter, J. D. 2007, CSE, 9, 90

Ishisaki, Y., Kelley, R. L., Awaki, H., et al. 2025, JATIS, 11, 042023

Kaastra, J. S. 2017, A&A, 605, A51

Kaastra, J. S., & Bleeker, J. A. M. 2016, A&A, 587, A151

Kinch, B. E., Schnittman, J. D., Kallman, T. R., & Krolik, J. H. 2016, ApJ, 826, 52

Kinch, B. E., Schnittman, J. D., Noble, S. C., Kallman, T. R., & Krolik, J. H. 2021, ApJ, 922, 270

Korista, K., Baldwin, J., Ferland, G., & Verner, D. 1997, ApJS, 108, 401

Krolik, J. H. 2001, ApJ, 551, 72

Laor, A. 1991, ApJ, 376, 90

Laor, A. 2003, ApJ, 590, 86

Lewis, K. T., Eracleous, M., & Storchi-Bergmann, T. 2010, ApJS, 187, 416

Lobban, A. P., Reeves, J. N., Porquet, D., et al. 2010, MNRAS, 408, 551

López, I. E., Yang, G., Mountrichas, G., et al. 2024, A&A, 692, A209

Lubiński, P., Beckmann, V., Gibaud, L., et al. 2016, MNRAS, 458, 2454

McKinney, W. 2010, in Proc. 9th Python in Science Conf., ed. S. van der Walt & J. Millman, 56

McKinney, W. 2011, in Python for High Performance and Scientific Computing, 14, 1

Miller, J. M., Behar, E., Awaki, H., et al. 2025, ApJL, 985, L41

Miller, J. M., Cackett, E., Zoghbi, A., et al. 2018, ApJ, 865, 97

Miller, J. M., Xiang, X., & Byun, D. 2025, arXiv:2510.20083

Molendi, S., Bianchi, S., & Matt, G. 2003, MNRAS, 343, L1

Molina, M., Reines, A. E., Latimer, L. J., Baldassare, V., & Salehirad, S. 2021, ApJ, 922, 155

Murphy, K. D., & Yaqoob, T. 2009, MNRAS, 397, 1549

Murray, N., & Chiang, J. 1997, ApJ, 474, 91

Naddaf, M.-H., Czerny, B., & Szczerba, R. 2021, ApJ, 920, 30

Negrete, C. A., Dultzin, D., Marziani, P., & Sulentic, J. W. 2012, ApJ, 757, 62

Nenkova, M., Sirocky, M. M., Nikutta, R., Ivezić, Ž., & Elitzur, M. 2008, ApJ, 685, 160

Nicastro, F. 2000, ApJL, 530, L65

Noda, H., Mori, K., Tomida, H., et al. 2025, PASJ, 77, S10

Pancoast, A., Brewer, B. J., Treu, T., et al. 2014, MNRAS, 445, 3073

Pozo Nuñez, F., Westhues, C., Ramolla, M., et al. 2013, A&A, 552, A1

Reefe, M., Sexton, R. O., Doan, S. M., et al. 2023, ApJS, 265, 21

Reynolds, C. S., & Begelman, M. C. 1997, ApJ, 488, 109

Schimoia, J. S., Storchi-Bergmann, T., Winge, C., Nemmen, R. S., & Eracleous, M. 2017, MNRAS, 472, 2170

Schnorr-Müller, A., Davies, R. I., Korista, K. T., et al. 2016, MNRAS, 462, 3570

Schnorr-Müller, A., Storchi-Bergmann, T., Nagar, N. M., & Ferrari, F. 2014, MNRAS, 438, 3322

Shi, F., Yuan, F., Li, Z., Su, Z., & Ji, S. 2024, ApJ, 970, 48

Shi, F., Zhu, B., Li, Z., & Yuan, F. 2022, ApJ, 926, 209

Shu, X. W., Yaqoob, T., & Wang, J. X. 2010, ApJS, 187, 581

Śniegowska, M., Marziani, P., Czerny, B., et al. 2021, ApJ, 910, 115

Storchi-Bergmann, T., Baldwin, J. A., & Wilson, A. S. 1993, ApJL, 410, L11

Storchi-Bergmann, T., Schimoia, J. S., Peterson, B. M., et al. 2017, ApJ, 835, 236

Strateva, I. V., Strauss, M. A., Hao, L., et al. 2003, AJ, 126, 1720

Strüder, L., Briel, U., Dennerl, K., et al. 2001, A&A, 365, L18

Tashiro, M., Watanabe, S., Maejima, H., et al. 2024, Proc. SPIE, 13093, 130931G

Tody, D. 1986, Proc. SPIE, 627, 733

Turner, M. J. L., Abbey, A., Arnaud, M., et al. 2001, A&A, 365, L27

Ulrich, M.-H., Maraschi, L., & Urry, C. M. 1997, ARA&A, 35, 445

Ursini, F., Marinucci, A., Matt, G., et al. 2015, MNRAS, 452, 3266

Virtanen, P., Gommers, R., Oliphant, T. E., et al. 2020, NatMe, 17, 261

Ward, C., Gezari, S., Nugent, P., et al. 2024, ApJ, 961, 172

Ward, C., Koss, M. J., Eracleous, M., et al. 2025, ApJ, 991, 116

Williams, P. R., Pancoast, A., Treu, T., et al. 2020, ApJ, 902, 74

Xrism Collaboration, Audard, M., Awaki, H., et al. 2024, ApJL, 973, L25

Yan, Z., & Xie, F.-G. 2018, MNRAS, 475, 1190

Yaqoob, T., George, I. M., Nandra, K., et al. 2001, ApJ, 546, 759